

## HIGH RESOLUTION STUDY OF PRESUPERNOVA CORE STRUCTURE

TUGULDUR SUKHBOLD<sup>1,2</sup>, S. E. WOOSLEY<sup>3</sup>, AND ALEXANDER HEGER<sup>4,5,6</sup>  
(Accepted —, 2018)  
– Oct, 2017

### ABSTRACT

The density structure surrounding the iron core of a massive star when it dies is known to have a major effect on whether or not the star explodes. Here we repeat previous surveys of presupernova evolution with some important corrections to code physics and four to ten times better mass resolution in each star. The number of presupernova masses considered is also much larger. Over 4,000 models are calculated in the range from 12 to 60  $M_{\odot}$  with varying mass loss rates. The core structure is not greatly affected by the increased spatial resolution. The qualitative patterns of compactness measures and their extrema are the same, but with the increased number of models, the scatter seen in previous studies is replaced by several localized branches. More physics-based analyses by Ertl et al. (2016) and Müller et al. (2016) show these branches with less scatter than the single parameter characterization of O’Connor & Ott (2011). These branches are particularly apparent for stars in the mass ranges 14 - 19  $M_{\odot}$  and 22 - 24  $M_{\odot}$ . The multi-valued solutions are a consequence of interference between several carbon and oxygen burning shells during the late stages of evolution. For a relevant range of masses, whether a star explodes or not may reflect more the small, almost random differences in its late evolution than its initial mass. The large number of models allow statistically meaningful statements about the radius, luminosity, and effective temperatures of presupernova stars, their core structures, and their remnant mass distributions.

*Subject headings:* stars: supernovae, evolution, black holes; nucleosynthesis; hydrodynamics

### 1. INTRODUCTION

As a massive star below the pair-instability threshold ( $\sim 80 M_{\odot}$ ; Woosley 2017) evolves through its final stages of nuclear burning, its central regions cool by neutrino emission, become degenerate, and tend to decouple from the overlying layers and evolve as separate stars. Although never becoming completely detached except for the lowest mass stars, the presupernova core takes on a structure similar to that of a white dwarf, mostly composed of iron, surrounded by a dense mantle of oxygen and intermediate mass elements. As numerous studies have shown, the structure of this configuration, and especially the rate at which the density declines outside the iron core is strongly correlated with the difficulty of blowing the star up (e.g., Burrows & Lattimer 1987; Fryer 1999). Recent studies have sought to capture this complex structure in just one or two parameters that might predict, albeit approximately, whether a star with a given mass blows up or collapses to a black hole simply from looking at one-dimensional models for stellar evolution (O’Connor & Ott 2011, 2013; Ugliano et al. 2012; Pejcha & Thompson 2015; Ertl et al. 2016; Sukhbold et al. 2016; Müller et al. 2016).

Sukhbold & Woosley (2014) discussed how the advanced burning stages, especially convective carbon and oxygen burning, sculpt this structure, and provided a library of presupernova stars consisting of 503 models in the mass range 12 to 65  $M_{\odot}$  to demonstrate the systematics and its dependence on input physics. Müller et al. (2016) prepared a larger grid of over 2,000 models between 10 and 32.5  $M_{\odot}$  and corrected some errors in Sukhbold & Woosley (2014). Their results showed finer structure, but similar global systematics (see especially their Fig. 6).

More recently, Farmer et al. (2016) using the MESA code, found that the choice of mass resolution, i.e., zoning, “*dominates the variations in the structure of the intermediate convection zone and secondary convection zone during core and shell hydrogen burning, respectively*” and greatly affects the structure of presupernova stars. They found that a minimum mass resolution of  $\sim 0.01 M_{\odot}$  was necessary to achieve convergence in the final helium core mass at the  $\sim 5\%$  level. They also found  $\sim 30\%$  variations in the central electron fraction and mass locations of the main nuclear burning shells, and that a minimum of  $\sim 127$  isotopes was needed to attain convergence of these values at the  $\sim 10\%$  level.

Renzo et al. (2017) also used the MESA code to explore the sensitivity of massive star evolution due to variations in the mass loss rate for stars with initial masses between 15 and 35  $M_{\odot}$ . They found variations in the presupernova core compactness parameter (§4.3) of  $\sim 30\%$  depending upon the choice of the algorithm. In a limited study of resolution in one model, they found roughly 9% variation in final core compactness, smaller than that resulting from uncertainties in mass loss prescription.

In this paper, we present a new survey similar to Sukhbold & Woosley (2014) and Müller et al. (2016), but

<sup>1</sup>Department of Astronomy, The Ohio State University, Columbus, OH 43210, USA, tuguldur.s@gmail.com

<sup>2</sup>Center for Cosmology and AstroParticle Physics, The Ohio State University, Columbus, OH 43210, USA

<sup>3</sup>Department of Astronomy and Astrophysics, University of California, Santa Cruz, CA 95064, woosley@ucolick.org

<sup>4</sup>Monash Center for Astrophysics, Monash University, Vic 3800, Australia, alexander.heger@monash.edu

<sup>5</sup>School of Physics & Astronomy, University of Minnesota, Minneapolis, MN 55455, U.S.A.

<sup>6</sup>Department of Astronomy, Shanghai Jiao-Tong University, Shanghai 200240, P. R. China.

using much finer zoning, a greater number of models and several different mass loss rates. The key differences of the new survey are listed in §2, including the correction to an erroneous pair-neutrino loss rate used by Sukhbold & Woosley (2014). §2 also offers a detailed discussion on the effects due to zoning, network size and the boundary pressure. In general, we find that the pattern of final core compactness seen in these previous studies is unaltered by finer zoning or larger reaction network, though the mass limits for different behaviors are shifted by about 10 % when the pair-neutrino loss rate is corrected. In §3 and §4 we discuss the general characteristics of the new survey, including its observable properties. With a much greater number of models, clear evidence emerges for multi-valued solutions to the presupernova structure of stars in the 14 - 19  $M_{\odot}$  and 22 - 24  $M_{\odot}$  ranges (see also Müller et al. 2016). In §5 we offer an interpretation for this feature through the physics of the advanced stage evolution in the cores of massive stars. Large variations in core structure are expected for stars of these masses no matter what resolution, mass loss rate, or reaction network is employed in the calculation (for the effects of such variations in individual models see Farmer et al. 2016; Renzo et al. 2017). Future surveys of supernova, as well as presupernova models should thus take care to examine, when feasible, a large number of masses in order to sample an outcome that is essentially statistical in nature. More specific results, and effects on explodability and remnant masses are discussed in §6. Finally, in §7 we offer our conclusions.

## 2. CODE PHYSICS AND ASSUMPTIONS

With several important exceptions the code, physics, and input parameters used here are the same as in Sukhbold & Woosley (2014) and Müller et al. (2016). The (solar) initial composition is from Asplund et al. (2009), as was used in Müller et al. (2016), but with an appropriate correction for the ratio  $^{15}\text{N}/^{14}\text{N}$  (Meibom et al. 2007). Convective and semi-convective settings, nuclear reaction rates, opacities, and mass loss rates are the same as in both of the earlier works. The mass range studied and lack of rotation are the same as well.

Nuclear burning was handled as usual, using a 19 isotope approximation network until the central oxygen mass fraction declines below 0.03 and a silicon quasi-equilibrium network with 121 isotopes (Weaver, Zimmerman, & Woosley 1978) thereafter. Numerous studies that compare this treatment with the energy generation and bulk nucleosynthesis obtained by “co-processing” with a network of several hundred to over 1,000 isotopes have shown excellent agreement (e.g., Woosley et al. 2002; Woosley & Heger 2007), at least up to central oxygen depletion where the switch to the quasi-equilibrium network is made. By co-processing, we mean carrying a large network in each zone using the same time step, temperature, and density, but not coupling the energy generation from that large network directly to the iterative loop within a time step. After oxygen depletion, the quasi-equilibrium network is more stable, contains the same weak interaction physics, and is roughly an order of magnitude faster. An exception is the treatment of oxygen and silicon burning in stars lighter than about 11  $M_{\odot}$  (Woosley & Heger 2015). For such light stars, it is important to follow neutronization in multiple off-

center shells where the quasi-equilibrium approximation has questionable validity and can be unstable. Such light stars are not part of the present survey which starts at 12  $M_{\odot}$ . §2.2 discusses the issue of network sensitivity in greater detail and confirms the validity of the approximation network plus quasi-equilibrium for representative cases.

Key differences in the new study are:

- The models in this paper employ much finer mass resolution (Fig. 1, Fig. 2, and Fig. 4). For the lightest stars considered (12  $M_{\odot}$ ), the increase is roughly a factor of four. Since an effort was made to keep fine resolution even in the larger stars, the factor for the highest masses considered, around 60  $M_{\odot}$ , was closer to fifteen. In the most massive models the total number of mass shells was approximately 16,000. Additional studies of individual cases of zoning sensitivity in 15  $M_{\odot}$  and 25  $M_{\odot}$  models (§2.1) showed little systematic difference. In all cases, zones contained less than about 0.01  $M_{\odot}$  everywhere, but were about ten times smaller than that in the heavy element core (Fig. 4). It is this core that is most critical in determining the final presupernova core properties, such as compactness. Surface zoning was a few times  $10^{-5} M_{\odot}$ , and all temperature and density gradients were well resolved (Fig. 2).
- A major, long standing coding error in the KEPLER code was repaired. The error affected the axial vector component of the pair neutrino losses. In particular, the error resulted in the accidental zeroing of the second term involving  $C'_A{}^2$  and  $Q_{\text{pair}}^-$  in the expression (Itoh et al. 1996, eq. 2.1)

$$Q_{\text{pair}} = \frac{1}{2}[(C_V^2 + C_A^2) + n(C_V'^2 + C_A'^2)]Q_{\text{pair}}^+ \quad (1)$$

$$+ \frac{1}{2}[(C_V^2 - C_A^2) + n(C_V'^2 - C_A'^2)]Q_{\text{pair}}^- \quad (2)$$

See Itoh et al. (1996) for the definitions of quantities. The consequence of this error was that the pair neutrino loss rate was underestimated by close to a factor of two during carbon burning and somewhat less during later, higher temperature stages. The error, introduced through an inadequate checking of a routine provided by email, was included in 2001, and affected all KEPLER calculations published through 2014. In particular it affected the often cited calculations of Woosley et al. (2002), Woosley & Heger (2007), and Sukhbold & Woosley (2014). Because some of the models from Sukhbold & Woosley (2014) were used by Sukhbold et al. (2016), it also affected the outcome of that work for masses larger than 14  $M_{\odot}$ . The bug was repaired, however, in the works of Woosley & Heger (2015) on 9  $M_{\odot}$ –11  $M_{\odot}$  stars and Woosley (2017) on pulsational pair instability supernovae. Most relevant to this present work, the bug was also repaired for the work of Müller et al. (2016). Because of the strong sensitivity of neutrino and nuclear reaction rates to temperature, the effect of the bug was a slight shift upwards in the burning temperature for the late stages of stellar evolution. For

a given model the change in presupernova structure was not great and, as we shall see, within the “noise” of other uncertainties. For the lightest models ( $< 14 M_{\odot}$ ) the difference is hardly noticeable, but it did systematically shift the outcome for a higher mass stars significantly downwards. For example, the peak in compactness that occurred for Sukhbold & Woosley (2014) at about  $24 M_{\odot}$  is shifted downwards in the work of Müller et al. (2016) and in the present work (§4) by about  $3 M_{\odot}$ .

- The surface boundary pressure is much less than in Müller et al. (2016), which significantly affects the final red supergiant (RSG) properties, but does not significantly alter the core structure. Whereas the mass loss rates are varied in the present study, the new calculations do not include Wolf-Rayet models where the envelope is completely lost. All stars studied here retained a substantial hydrogen envelope when they died.

### 2.1. The Effects of Zoning

One criterion for adequate zoning is that key variables like temperature and density be well resolved, that is, that they do not vary greatly in going from zone “i” to “i+1”. Stellar evolution codes solve linear approximations to non-linear differential equations. Fig. 2 shows the resolution for a standard  $M_{\text{ZAMS}} = 15 M_{\odot}$  presupernova star with 4225 zones. The figure gives the scale heights in Lagrangian units (solar masses here) for the temperature and density. Pressure and other derived quantities, though not plotted, show similar variation. The scale height, e.g., for density is defined as  $M_{\rho} = dm/d \ln \rho$ . In places, this quantity can abruptly become artificially small because of discontinuous changes in mean atomic weight at the edges of convective shells. Some of the prominent downward spikes in the iron core are where partial photodisintegration has changed  $\bar{A}$  appreciably. These abrupt changes in  $\bar{A}$  are responsible for most of the discontinuous spikes in the figure. Large upward spikes indicate regions of near constant temperature or density. An especially large spike near the center of the presupernova star reflects a temperature inversion (note that the scale height can be either positive or negative; the absolute value is plotted). Where the derivative changes sign and passes through zero, a spike results.

The figure shows that there are roughly 100 to 1000 zones per scale height everywhere in the star, except in the steep gradient at the edge of the helium core, where the actual density varies by six orders of magnitude over an interval of  $\sim 0.2 M_{\odot}$ . Here the zoning is worst. In one location, the density changes by a maximum of 30% from one zone to the next. Zone masses here were  $\sim 5 \times 10^{-4} M_{\odot}$ . Because this location moves in mass as the star evolves, still finer zoning would have significantly lengthened the calculation. We conclude that the relevant physical quantities are well resolved in the new study. In fact, except at the edge of the helium core, they are over-resolved. This was done in order to explore the sensitivity of outcome, e.g., the extent of convective shells, and to see if fine zoning alone would lead to a “converged” answer.

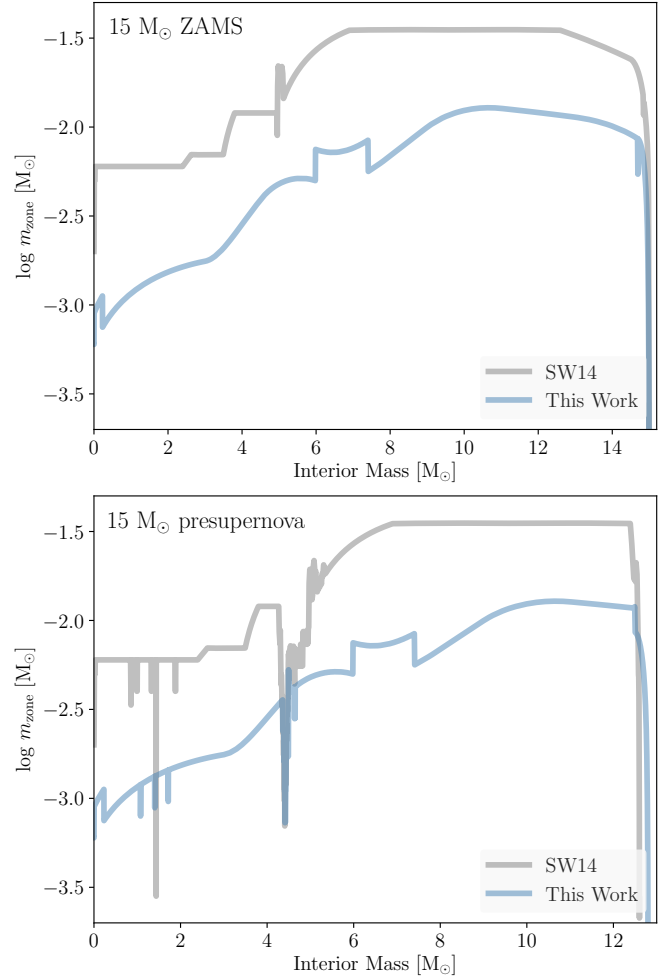


FIG. 1.— The masses of individual zones as a function of interior mass for a  $15 M_{\odot}$  zero age main sequence star (top) and the corresponding presupernova star (bottom). The gray curves are the zoning for the earlier model of Sukhbold & Woosley (2014, SW14) which was very similar to that of Woosley & Heger (2007), Sukhbold et al. (2016) and Müller et al. (2016); the blue curves are for the new survey reported here. The previous ZAMS model had 1,068 zones, the new one, 4,257. Stars are continually rezoned as they run to accommodate changing gradients in key quantities, but the zoning shown here did not vary greatly, with the exception of fine zones added at the base of the hydrogen envelope around  $4.4 M_{\odot}$ , and a few regions of finer zoning at what were once the boundaries of convective shells inside  $2 M_{\odot}$ . The surface zoning was  $\sim 10^{28}$  g in all studies (§2).

Convergence assumes the existence of a well-defined solution to the stellar structure equations. As the numerical resolution is increased, if the subgrid physics (e.g., convection) is coded in a zoning independent way, the answer from a given calculation should approach this solution and give a constant answer. Certainly it is possible for a stellar model to be inadequately zoned. Envision Fig. 2 with zoning of  $0.1 M_{\odot}$ . No one today would think of trying to use just a few hundred zones in a presupernova model for a  $25 M_{\odot}$  star, though substantial progress was once made that way (Weaver, Zimmerman, & Woosley 1978). But given the power of modern machines, how many zones are enough?

Typical KEPLER models by Sukhbold & Woosley (2014) and Müller et al. (2016) used about 1,200 zones, roughly independent of the star’s total mass, though the zon-

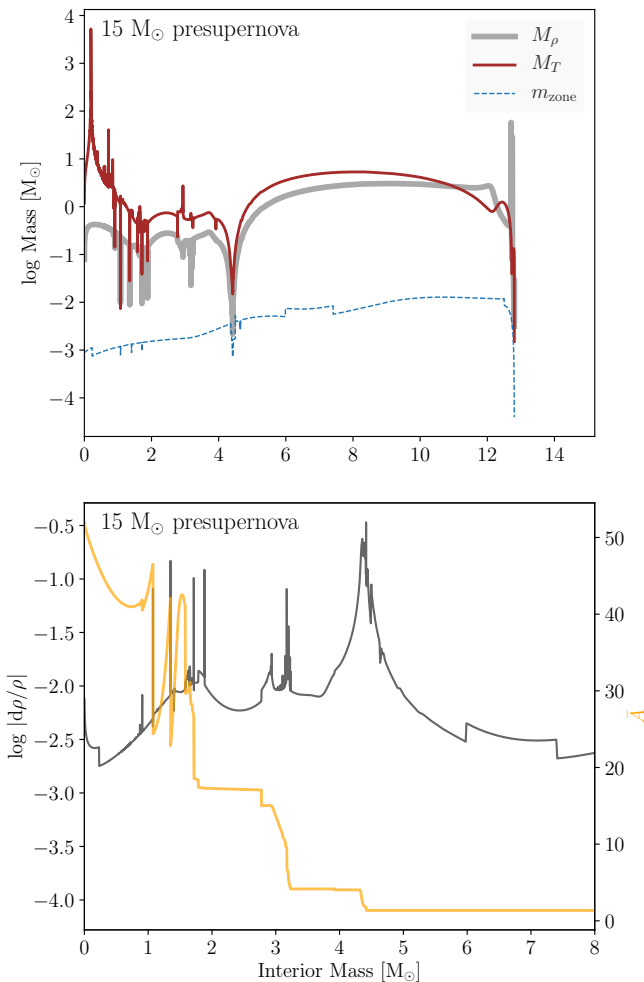


FIG. 2.— Density and temperature resolution in the same  $15 M_{\odot}$  presupernova model shown in the lower panel of Fig. 1. The top panel shows the scale heights ( $M_x \equiv dm/d \ln x$ ) expressed in solar masses for the density ( $M_{\rho}$ ; grey curve) and temperature ( $M_T$ ; red curve). The blue dashed curve shows the zoning. The bottom panel shows the actual variation in density between zones and mean atomic weight,  $\bar{A}$ , plotted also as a function of interior mass. Discontinuities in  $\bar{A}$  occur at the boundaries of active and fossil convective shells causing abrupt changes in density that the code attempts to resolve. The large spike in  $M_T$  at  $0.15 M_{\odot}$  reflects a temperature inversion at the star’s center (where  $dT/dm$  is negative) and a small region of nearly constant temperature bounding it. Both panels show that temperature and density gradients are very well resolved throughout the star, except perhaps in the very steep density gradient at the edge of the helium core ( $4.33 M_{\odot}$ ), where changes of up to 30% occur for the density in a few zones.

ing was by no means uniform. Zones were concentrated at the center, where temperature-dependent burning required fine resolution, in the steep density gradient at the base of the red giant convective envelope, and at the surface. Continuous rezoning kept gradients in density, temperature, and zone radius well resolved. For a large range of masses, characteristics of the presupernova star, such as its helium, carbon, and iron core masses, its luminosity and radius, and its “compactness” varied smoothly with mass and were consistent with numerous past studies. In some mass ranges, however, especially in the range  $14 M_{\odot}$  to  $19 M_{\odot}$ , the compactness parameter often varied wildly. These variations were attributed by Sukhbold & Woosley (2014) to the interaction of convective carbon and oxygen burning shells. The character-

istics of those burning shells were irregular in location, extent, duration, and intensity, and so, for some masses, was the final presupernova core structure. But might some of that variation also be attributed to inadequate resolution? Would a set of finer-zoned models show less variation, or reveal structure in the noise?

Most of this paper is about the results of repeating the survey of Sukhbold & Woosley (2014) with finer zoning (Fig. 1). In this section, however, we briefly examine, for just four masses, the question: “What is enough?” In part, the answer must have a pragmatic aspect. If running with 3,000 and 30,000 zones gives answers that differ in some important quantity by 5%, but if changing the stellar mass by  $0.01 M_{\odot}$ , or some bit of uncertain stellar physics by a small fraction of its error bar alters the answer by 50%, perhaps 3,000 zones is “good enough.” Resources would be better spent studying the variations that depend on these other variables.

There is a deeper issue though when the answer is deterministic, but unpredictable. It is an inherent aspect of chaos that tiny changes upstream produce large differences in outcome. As the noted chaos theorist Edward Lorenz once said “*Chaos exists when the present determines the future, but the approximate present does not approximately determine the future*”<sup>7</sup>. As noted by Sukhbold & Woosley (2014) and Müller et al. (2016) and, as will be explored in greater depth here, for some ranges of mass, presupernova evolution is like that. Seemingly minuscule changes in initial conditions may determine whether a star in an important mass range explodes as a supernova or collapses to a black hole. How different could two outcomes be?

Table 1 gives the final presupernova properties of four sets of models with varying resolution for initial masses of  $15.00$ ,  $15.01$ ,  $25.00$ , and  $25.01 M_{\odot}$ . The spatial resolution ranges from about 1,200 to 16,000 mass shells. The most finely resolved models used roughly twice as many timesteps to reach the presupernova stage as the least resolved models. The “compactness” parameter,  $\xi_{2.5}$  (O’Connor & Ott 2011) is inversely proportional to the radius enclosing innermost  $2.5 M_{\odot}$  of the presupernova core, while  $M_4$  and  $\mu_4$  (Ertl et al. 2016, further discussed in §4.3) are, respectively, the lagrangian location of the mass shell with entropy per baryon  $s = 4 k_B$  and the derivative of mass at that location evaluated over a mass interval of  $0.3 M_{\odot}$ . The motivation for using these parameters is discussed in §4.3.

The zoning for the typical  $15 M_{\odot}$  case in Fig. 1 corresponds to the moderately zoned case (15.00D) in Table 1. Initial zoning in other  $15.00 M_{\odot}$  and  $15.01 M_{\odot}$  cases was scaled at all locations in the star by roughly factors of two. For the  $25.00 M_{\odot}$  and  $25.01 M_{\odot}$  models the number of zones was proportionately larger. That is Model 25.00C had roughly 25/15 as many zones as Model 15.00C, etc. There was no Model 25.00F, instead there was a Model 25.00A which had about half the zoning of 25.00B. The continuous rezoning parameters were set so as to preserve, within about 10%, the initial zoning. The number of zones given in Table 1 is for the presupernova star.

Two closely adjacent masses were studied at  $15 M_{\odot}$

<sup>7</sup> [mpe2013.org/2013/03/17/chaos-in-an-atmosphere-hanging-on-a-wall](http://mpe2013.org/2013/03/17/chaos-in-an-atmosphere-hanging-on-a-wall)

TABLE 1  
PRESUPERNOVA PROPERTIES WITH VARYING RESOLUTION AND MASS

$M_{\text{ZAMS}}$ [ $M_{\odot}$ ]	$N_{\text{zones}}$	$N_{\text{steps}}$	$M_{\text{presSN}}$ [ $M_{\odot}$ ]	$L_{\text{presSN}}$ [ $10^{38}$ ergs $s^{-1}$ ]	$R_{\text{presSN}}$ [ $10^{13}$ cm]	$T_{\text{eff,presSN}}$ [K]	$M_{\text{He}}$ [ $M_{\odot}$ ]	$M_{\text{Fe}}$ [ $M_{\odot}$ ]	$\xi_{2.5}$	$M_4$ [ $M_{\odot}$ ]	$\mu_4$
15.00B	1258	59992	12.935	3.57	6.04	3425	4.309	1.552	0.152	1.665	0.079
15.00C	2153	60162	12.866	3.58	5.97	3450	4.314	1.580	0.178	1.680	0.089
15.00D	4225	63435	12.804	3.59	6.06	3420	4.326	1.581	0.176	1.718	0.085
15.00E	8138	77578	12.485	3.69	6.19	3410	4.409	1.494	0.094	1.496	0.044
15.00F	15912	87612	11.717	4.02	6.64	3363	4.683	1.413	0.111	1.591	0.047
25.00A	874	38558	16.047	7.88	8.56	3505	8.342	1.609	0.303	1.915	0.103
25.00B	1885	38202	16.026	9.59	9.78	3445	8.351	1.620	0.301	1.911	0.102
25.00C	3358	40799	15.690	9.72	9.79	3455	8.427	1.606	0.301	1.916	0.102
25.00D	6515	45929	15.902	9.59	9.77	3445	8.382	1.630	0.301	1.910	0.102
25.00E	12734	58975	15.816	9.70	9.85	3440	8.432	1.643	0.303	1.903	0.104
15.01B	1260	59794	12.922	3.59	6.05	3425	4.319	1.561	0.164	1.675	0.083
15.01C	2149	60641	12.701	3.64	6.05	3435	4.361	1.513	0.189	1.742	0.088
15.01D	4190	63675	12.574	3.67	6.16	3410	4.386	1.357	0.126	1.457	0.067
15.01E	8103	76827	12.157	3.83	6.37	3390	4.523	1.506	0.100	1.517	0.046
15.01F	15952	77854	11.845	3.95	6.55	3373	4.638	1.438	0.159	1.599	0.070
25.01A	876	38416	16.138	7.88	8.56	3505	8.269	1.606	0.301	1.911	0.102
25.01B	1897	38165	16.319	9.57	9.80	3440	8.348	1.610	0.298	1.909	0.101
25.01C	3335	41211	15.141	9.85	9.82	3460	8.498	1.613	0.300	1.910	0.101
25.01D	6466	46494	15.235	9.81	9.89	3445	8.485	1.606	0.302	1.907	0.103
25.01E	12268	67699	13.264	10.34	9.86	3495	8.720	1.600	0.315	1.901	0.110

NOTE. — All quantities are measured at the presupernova stage.  $N_{\text{zones}}$  is slightly larger at the beginning of calculation.

and  $25 M_{\odot}$  in order to compare the effects of fine zoning with slight variations in any other parameter of the problem. One might have chosen instead to vary time step, overshoot, the rate for  $^{12}\text{C}(\alpha, \gamma)^{16}\text{O}$ , semiconvection, mass loss, or rotation. Although no substitute for a full survey of such dependencies, varying the mass slightly in a situation where the solution is chaotic might be expected to send the calculation down one path or another. Stated another way, if varying the mass by less than 0.1 % results in an answer significantly different than one obtained by increasing the zoning by a factor of two, perhaps there is no reason to use much finer zoning for that mass. On the other hand, if all models give the same answer, one might have confidence in the uniqueness of that model, at least for an assumed set of stellar physics.

The two choices,  $15 M_{\odot}$  and  $25 M_{\odot}$ , illustrate these two possibilities nicely. In all cases the observable properties of the presupernova star, its luminosity and radius, and hence its effective temperature, are well determined. Changing opacities, composition, etc., would certainly cause variation, but the bulk observables of our models are well determined. There is a weak, but noticeable trend to produce smaller presupernova stellar masses and larger helium core masses when the zoning is finer. As will be discussed later, this is a consequence of variation in the time spent as a red or blue supergiant, which, in turn, is sensitive to an uncertain treatment of semiconvection. A small number of episodic mixing events at the edge of convective hydrogen burning core can temporarily “rejuvenate” the core and by affecting the gravitational potential of hydrogen burning shell, eventually causing the transition from blue to red to occur at different times. This trend does not emerge because the models are converging with higher resolution, but rather as a result of enhanced mixing due to the uncertain treatment of convection physics.

The measures of presupernova core structure on the

other hand vary by factors of two for the  $15 M_{\odot}$  models, but scarcely at all for the  $25 M_{\odot}$  models. The reasons for the difference will be discussed in §5, but we note that any reasonable zoning suffices to get the structure of the  $25 M_{\odot}$  correct, but no reasonable zoning shows convergence for the  $15 M_{\odot}$  model. Not knowing beforehand what the outcome will be for an arbitrary mass, we used here the maximum zoning that time and the desire to survey thousands of models allowed. This is most like the “D” models in Table 1. There is little motivation, however, for carrying out still finer resolution studies when a trivial change in mass,  $15.00 M_{\odot}$  to  $15.01 M_{\odot}$ , causes more variation than an order of magnitude increase in zoning.

## 2.2. The Effects of Networks

Uncertainty in nuclear energy generation and neutronization during the various episodes of burning can be another source of variability in presupernova models. In this section the effect of using either the standard 19-isotope approximation network plus silicon quasiequilibrium (§2) or a much larger nuclear reaction network is explored. It should be noted that while the standard network carries the abundances of only 19 species, it has the power of a network roughly twice that size since reactions through trace species like  $^{23}\text{Na}$ ,  $^{27}\text{Al}$ , etc. are carried in a steady-state approximation (Weaver, Zimmerman, & Woosley 1978). Reactions coupling  $^{54}\text{Fe}$  to  $^{56}\text{Ni}$  are also included, as are approximations to energy generation by the CNO- and pp-cycles and to  $^{14}\text{N}(\alpha, \gamma)^{18}\text{F}(e^+\nu)^{18}\text{O}(\alpha, \gamma)^{22}\text{Ne}$ <sup>8</sup>.

The large network used for comparison here is drawn from an extensive nuclear data base maintained and used for nucleosynthesis studies for decades (e.g., Woosley et al. 2002). Key reaction rates such as  $^{14}\text{N}(p, \gamma)^{15}\text{O}$ ,  $3\alpha$ ,

<sup>8</sup> In the code,  $^{14}\text{N}$  is converted to  $^{20}\text{Ne}$  at an appropriate rate conserving mass.

$^{12}\text{C}(\alpha, \gamma)^{16}\text{O}$ , the  $(\alpha, \gamma)$  and  $(\alpha, p)$  reactions on  $\alpha$ -nuclei and the weak interaction rates are the same in both networks. The network is “adaptive” (Rauscher et al. 2002) in the sense that isotopes are added or subtracted at each step to accommodate the reaction flow (e.g., there is no need to include a detailed network for the iron group during hydrogen burning). Usually the settings on the network size are quite liberal, resulting in from 700 to 1,200 isotopes being carried in the early and late stages of evolution respectively (Woosley & Heger 2007). Here, because we are only interested in stellar structure and not, e.g., the  $s$ -process, a smaller number was carried, typically 300 isotopes extending up through the element Selenium. All of the iron-group isotopes in the quasi-equilibrium network were included, and many more, so that core neutronization during and after silicon burning was equivalently calculated.

Network sensitivity was examined for four different masses of star, 15.00, 15.01, 25.00, and 25.01  $M_{\odot}$ . Two studies were carried out to test network sensitivity. Table 2 edits the evolution of the 15.00 star, similar to Model 15.00D in Table 1, at different times in its evolution using 3 approximations to the energy generation and neutronization. The APPROX case corresponds to using the 19 isotope approximation network and quasiequilibrium network, as is standard in the rest of this paper. The COPROC case carries the large network of about 300 isotopes along with the approximation network in “co-processing mode”. That is, the approximation and quasiequilibrium networks are used for energy generation in the stellar structure calculation, but the network is also carried along in passive mode. The same time step is used at the same temperature and density to evolve, zone by zone, a much larger number of isotopes in parallel with the approximation network. Sub-cycling is done within a given time step to follow the abundances of trace isotopes accurately. Coprocessing is only performed in the code up to the point where the transition to quasiequilibrium occurs in a zone, typically at oxygen depletion  $X(^{16}\text{O} = 0.03)$ . The output from the large co-processing network is used to continually update the electron mole number,  $Y_e$ , which feeds back into the structure calculation. Because  $Y_e$  evolves slowly, no iteration is required. The energy generation from the large network can also be used to check the validity of the approximation network, though no correction is applied. In the third case FULL, the big network is coupled directly to the structure calculation throughout the entire life of the star, including silicon burning and core collapse. This might be deemed the most accurate approach, but it is slow, requiring an order of magnitude more computer resources, and prone to instability during silicon burning because of strongly coupled flows.

In Table 2, up until oxygen depletion, two different numbers are given for the co-processing run (COPROC). The first is the energy generation from the approximation network, which is used to calculate the stellar model, and the second is the output from the passively carried big network. Hydrogen burning and depletion correspond to central hydrogen mass fractions of 0.4 and 0.01. Helium burning and helium depletion are when the central helium mass fraction is 0.5 and 0.01. Carbon “ignition” is actually evaluated during the Kelvin-Helmholtz contraction between helium depletion and real carbon burning

when the central temperature is  $5 \times 10^8$  K, and carbon depletion is when the central carbon mass fraction is 1%. Similarly, “oxygen ignition” is when the central temperature during Kelvin-Helmholtz contraction is  $1.5 \times 10^9$  K and oxygen has yet to burn, and oxygen depletion is when the central oxygen mass fraction is 0.03. Silicon ignition is at  $3.0 \times 10^9$  K, and silicon depletion is when the silicon mass fraction is 1%. Presupernova is when the core collapse speed exceeds a maximum of  $900 \text{ km s}^{-1}$ .

The table shows near exact agreement in energy generation and  $Y_e$  calculated using all three approaches until at least oxygen ignition. The slight differences in energy generation at carbon ignition do not matter because neutrino losses (far right column) dominate at the time examined. By oxygen depletion though, things are starting to mildly diverge. This divergence has three causes. One is the electron capture that goes on in the late stages of oxygen burning and starts to appreciably affect  $Y_e$ . This change is not followed by the APPROX network. Carrying  $Y_e$  in the co-processing run addresses most of this divergence; the values of  $Y_e$  in the co-processing and full network runs are nearly the same. Another effect, more difficult to disentangle, is the fact that, at late times, the stellar structure in the different calculations starts to diverge. It diverges, in part, of the different nuclear physics, but even more because of the chaotic nature of the evolution. As was seen in the zoning study (§2.1), in certain initial mass ranges two models with even slightly different physics will differ appreciably in final outcome. The third effect is the instantaneous difference due solely to the differing treatments of nuclear physics. This is what we are actually trying to study, but difficult to separate from cumulative effects due to structural changes. Even so, at silicon depletion the three values of  $Y_e$  agree very well and the energy generation differs by a factor of two, which is mostly due to the higher temperature in the APPROX case and the very sensitive temperature dependence of the silicon burning reactions.

These small differences probably cause very little change in the presupernova model because the star has a certain amount of fuel to burn and the total energy release is set by known nuclear binding energies. The different burning rates only affects modestly the temperature at which the silicon burns in steady state (Woosley et al. 2002). We conclude that the approximation plus quasiequilibrium approach is adequate for our survey and introduces errors that are small compared with other variations that occur when other uncertain quantities, or even the zoning change.

Table 3 examines the effect of using either the large network or the approximation network plus quasiequilibrium to study stars of 15.00, 15.01, 25.00, and 25.01  $M_{\odot}$ , the same masses considered in the zoning sensitivity study (§2.1). Only one zoning was considered here, but the resolution was about three times greater in all 4 cases than in Sukhbold & Woosley (2014). Fewer time steps were taken during hydrogen burning than in the zoning sensitivity study. An overall limit of  $5 \times 10^{10}$  s was placed on the time step as opposed to  $1 \times 10^{10}$  s in the survey and zoning sensitivity study. Here, the emphasis is on comparing runs with different networks, not on the highest spatial and temporal resolution. Consequently the 15.00 model in Table 3 is not directly comparable

TABLE 2  
CENTRAL PROPERTIES FOR DIFFERENT NETWORK  
TREATMENTS FOR 15.00  $M_{\odot}$  MODEL

network	$\log T_c$ [K]	$\log \rho_c$ [g cm $^{-3}$ ]	$Y_{e,c}$	$\log S_n$ [ergs g $^{-1}$ s $^{-1}$ ]	$\log  S_{\nu} $
H burning					
APPROX	7.564	0.822	0.70042	5.104	3.910
COPROC	7.564	0.822	0.70196	5.104	3.910
FULL	7.565	0.820	0.69991	5.109	3.914
H depletion					
APPROX	7.676	1.138	0.50581	5.376	4.114
COPROC	7.676	1.138	0.50616	5.376	4.114
FULL	7.677	1.136	0.50489	5.387	4.129
He burning					
APPROX	8.249	3.127	0.49998	5.600	1.375
COPROC	8.250	3.123	0.49932	5.621	1.383
FULL	8.249	3.122	0.49932	5.621	1.371
He depletion					
APPROX	8.406	3.426	0.49998	5.624	2.560
COPROC	8.406	3.426	0.49932	5.627	2.562
FULL	8.407	3.422	0.49932	5.667	2.577
C ignition					
APPROX	8.703	4.544	0.49998	0.405	4.750
COPROC	8.704	4.546	0.49933	0.434	4.756
FULL	8.700	4.513	0.49933	0.368	4.729
C depletion					
APPROX	9.081	6.602	0.49998	6.193	8.198
COPROC	9.080	6.598	0.49894	6.181	8.202
FULL	9.079	6.580	0.49897	6.108	8.212
O ignition					
APPROX	9.176	6.895	0.49998	10.63	9.123
COPROC	9.176	6.899	0.49896	10.60	9.116
FULL	9.176	6.944	0.49899	10.58	9.188
O depletion					
APPROX	9.343	7.056	0.49998	11.53	11.05
COPROC	9.346	7.037	0.49242	11.60	11.12
FULL	9.352	6.990	0.49242	11.64	11.27
Si ignition					
APPROX	9.477	8.068	0.48679	12.14	11.21
COPROC	9.477	8.087	0.48609	12.18	11.19
FULL	9.477	8.084	0.47945	11.51	11.29
Si depletion					
APPROX	9.583	7.699	0.47060	12.71	13.01
COPROC	9.571	7.706	0.46987	12.67	12.97
FULL	9.477	7.739	0.46809	12.40	12.92
presupernova					
APPROX	9.885	9.747	0.43848	(16.11)	16.24
COPROC	9.880	7.762	0.43747	(16.09)	16.20
FULL	9.869	10.10	0.43266	(16.83)	16.94

NOTE. —  $S_n$  is the energy generation rate excluding neutrino-losses, and is negative during the presupernova stage due to photodisintegration. Values in parentheses denote  $\log |S_n|$ . The two values of  $Y_{e,c}$  and  $S_n$  given for co-processing calculations until core oxygen depletion (until quasi-equilibrium) are from approximation network (top) and co-processed big network (bottom).

with the one in Table 1.

Table 3 gives, in addition to the presupernova zoning and time steps, the masses of the iron, carbon-oxygen, and helium cores, the central mass fraction of carbon evaluated just prior to carbon ignition, the central value of the electron mole number,  $Y_e$  in the presupernova star, and the descriptors of presupernova core structure,  $\xi_{2.5}$ ,  $\mu_4$ , and  $M_4$ . Though not given, the presupernova masses,

radii, luminosities, and effective temperatures are in the same range as for the same mass stars in Table 1.

Based solely on the changes in the core structure and iron core mass for the 15.00 and 15.01  $M_{\odot}$  models, one might conclude that using a large network made a substantial difference and all future runs should take much greater care with the nuclear physics. Though the models do indeed differ, this would not be a valid inference. As shown in §2.1 and discussed elsewhere in the paper, changing *anything* for models in some mass ranges can give qualitatively different answers for core structure. The differences between runs with large and small networks is within the range of differences resulting from increased or decreased zoning (Table 1) or a small change in the star’s mass. More telling is the fact that the central carbon abundances, the helium and carbon-oxygen core masses, and most critically the central value of  $Y_e$  all agree very well. The approximation network is doing a fine job representing the nuclear physics. It is just that other, uncontrollable factors introduce large variations in the core structure of a 15  $M_{\odot}$ , and to a lesser extent 25  $M_{\odot}$  star. We conclude that the 19-isotope approximation network and quasiequilibrium hypothesis are quite adequate for surveys like this. Instead, focus should be placed on studying the impact of stellar physics on the statistical properties over the entire mass range.

### 2.3. Boundary Pressure

Especially during its post-main sequence evolution, the radius of a model star is sensitive to surface boundary conditions. Different codes treat the surface in different ways. Many use a boundary condition on pressure or density that sometimes includes a reduction of gravity by the Eddington factor and by the inertia term from wind acceleration (e.g., Appenzeller 1970; Heger 1998; Paxton et al. 2015). Others solve the wind equation for conditions at the sonic radius (Grassitelli, private communication, 2018). Still others fit the surface to a stellar atmosphere of varying complexity (e.g. plane-parallel gray or tables) (e.g. Paxton et al. 2011; Chieffi & Straniero 1989). KEPLER uses a constant boundary pressure,  $P_{\text{bound}}$  that does not vary during the evolution. The advantage of such an approach is its simplicity, but care must be taken that  $P_{\text{bound}}$  is not so large as to greatly alter the solution.

Ideally,  $P_{\text{bound}}$  only influences the structure of a tiny mass near the surface. No reasonable value of  $P_{\text{bound}}$  affects main sequence evolution, for example, because the the pressure gradient there is very steep. The gradient becomes shallower during the RSG phase though, and even slightly different radii there can significantly alter the mass loss rate. The timing and development of the surface convection zone is also affected. Both can have a significant affect on the star’s location in the HR-diagram and, to a lesser extent, the helium core mass and presupernova structure. Traditionally, studies with KEPLER have used  $P_{\text{bound}} = 50$  to 100 dyne cm $^{-2}$  (e.g., Woosley et al. 2002; Woosley & Heger 2007; Sukhbold & Woosley 2014). An exception is the work of Müller et al. (2016), where a much larger value,  $\sim 3500$  dyne cm $^{-2}$  was used.

In the present study a value of 50 dyne cm $^{-2}$  is employed. Is this low enough? To explore the sensitivity of results to boundary pressure, a standard 15.00  $M_{\odot}$ , Model S15.00D in Table 1, was calculated using a vari-



TABLE 3  
PRESUPERNOVA PROPERTIES WITH VARYING NETWORK SIZE

$M_{ZAMS}$ [ $M_{\odot}$ ]	network	$N_{zones}$	$N_{steps}$	$M_{He}$ [ $M_{\odot}$ ]	$M_{CO}$ [ $M_{\odot}$ ]	$^{12}C_{ign}$	$M_{Fe}$ [ $M_{\odot}$ ]	$\xi_{2.5}$	$M_4$ [ $M_{\odot}$ ]	$\mu_4$	$Y_{e,c}$
15.00	APPROX	4233	32013	4.319	2.949	0.215	1.527	0.187	1.760	0.087	0.438
15.00	COPROC	4227	33294	4.319	2.946	0.215	1.537	0.179	1.742	0.084	0.437
15.00	FULL	4185	39361	4.383	3.014	0.202	1.407	0.139	1.469	0.068	0.433
15.01	APPROX	4235	33091	4.308	2.937	0.211	1.373	0.143	1.449	0.088	0.434
15.01	COPROC	4248	35736	4.298	2.925	0.216	1.387	0.135	1.421	0.097	0.432
15.01	FULL	4194	36083	4.390	2.998	0.214	1.511	0.195	1.761	0.089	0.437
25.00	APPROX	4717	30080	8.663	6.711	0.179	1.604	0.311	1.913	0.107	0.444
25.00	COPROC	4721	30143	8.670	6.722	0.180	1.580	0.306	1.891	0.106	0.443
25.00	FULL	4589	42642	8.179	6.322	0.179	1.806	0.240	1.807	0.084	0.438
25.01	APPROX	4696	30317	8.633	6.720	0.176	1.617	0.312	1.912	0.108	0.444
25.01	COPROC	4681	30120	8.640	6.670	0.176	1.564	0.289	1.854	0.110	0.443
25.01	FULL	4531	43698	8.411	6.513	0.180	1.835	0.252	1.837	0.088	0.438

NOTE. — All quantities are measured at the presupernova stage, except  $^{12}C_{ign}$  (§2.2).  $N_{zones}$  is slightly larger at the beginning of calculation.  $Y_{e,c}$  is evaluated at the center.

ety of boundary pressures from 10 to 6400 dyne  $cm^{-2}$  maintained throughout the evolution. The resulting HR diagrams and radial histories are shown in Fig. 3. For  $P_{bound} \lesssim 500$  dyne  $cm^{-2}$  the trajectory in the HR-diagram is essentially identical for six different choices of  $P_{bound}$ . The presupernova radius and luminosity do not vary. For larger values of  $P_{bound}$  though, especially  $P_{bound} \gtrsim 1000$  dyne  $cm^{-2}$  significant variation is found.

Even the models with small surface pressures show some variation in final properties. For example, for  $P_{bound}$  between 10 and 400 dyne  $cm^{-2}$  the final star mass varied between 12.59  $M_{\odot}$  and 12.61  $M_{\odot}$ , while the helium core mass varied between 3.61  $M_{\odot}$  and 3.67  $M_{\odot}$ . Some of this variation is a consequence of the irreducible noise in running any model twice with even small variations in the physics or mass, but part could be a residual sensitivity to  $P_{bound}$ .

Closely related to the treatment of surface boundary conditions is surface zoning. In our recent studies (Sukhbold & Woosley 2014; Müller et al. 2016), rezoning was allowed to continue all the way to the surface of the star throughout its evolution. This often resulted in coarse zoning near the photosphere during the RSG stage. Fine zoning on the main sequence was lost to de-zoning when the temperature and density gradients were shallow. See Fig. 1 for a sample comparison with the older model. In the new models rezoning was not allowed in the outer 250 zones, typically 0.3  $M_{\odot}$ . Thus the fine surface zoning shown in Fig. 1 was maintained throughout the evolution for all models. Typical zoning near the surface is less than  $5 \times 10^{-4} M_{\odot}$ .

The use of finer surface zoning and a reduced boundary pressure generally gave larger radii and increased mass loss during the RSG stage, especially as compared with Müller et al. (2016). Because the helium core mass was not appreciably affected though, the final core compactness, nucleosynthesis, and remnant masses are not altered by this change.

### 3. THE NEW SURVEY

Three grids of models were calculated for initial main sequence masses in the range 12 through 60  $M_{\odot}$  using the zoning described in §2 and three choices of mass loss rate. Since all stars retained at least a small envelope

mass as presupernova stars, the relevant mass loss rate was that of Nieuwenhuijzen & de Jager (1990). The first set of models uses that rate unmodified ( $\dot{M}_N$ ). This results in so much of the envelope being lost by stars above about 27  $M_{\odot}$ , that the residual envelope, typically a few solar masses, becomes unstable and develops density inversions of more than an order of magnitude. We suspect that massive stars with extremely large radii and low mass envelopes become unstable in nature at this point and lose their remaining hydrogen rapidly (e.g., Sanyal et al. 2015, 2017). Mass loss is not the focus here though. In order to have a greater range of helium core masses, a second set of models used one-half of the standard mass loss ( $\dot{M}_N/2$ ) appropriate for solar metallicity and encountered no instability up to 40  $M_{\odot}$ . Finally, a third set was calculated with one-tenth the standard mass loss ( $\dot{M}_N/10$ ) to provide a sparse mass grid between 12  $M_{\odot}$  and 60  $M_{\odot}$ . Considering that mass loss prescriptions are probably uncertain (Renzo et al. 2017; Beasor & Davies 2018), the factors of two and ten could reflect a sensitivity study, or they might be appropriate for stars with reduced metallicity.

Altogether 1,499 models were calculated in the mass range 12 to 27  $M_{\odot}$  using the standard mass loss rate and 2,799 models from 12 to 40  $M_{\odot}$  using half that value. The grid spacing was 0.01  $M_{\odot}$  for both sets. The third set with one-tenth the standard mass loss rate, consisted of only 49 models between 12 and 60  $M_{\odot}$  with a mesh size of 1  $M_{\odot}$ . Lower metallicity stars were not considered but, except for zero, metallicity would have affected the answer chiefly by changing the mass loss and hence hydrogen envelope mass of the presupernova star. As we shall see, the helium core mass is not entirely independent of the remaining envelope mass, but it is insensitive.

The code was compelled to spend a much greater number of time steps during hydrogen and helium burning by imposing a limit on the maximum time step of  $10^{10}$  s. A minimum of roughly 10,000 steps was thus spent burning hydrogen on the main sequence. This helped to weaken the impact of random semiconvective mixing events that affected the final envelope mass and, to a smaller extent, the helium core mass. It also improved the accuracy of the treatment of convection and burning as “split” operations (convection and burning are not implicitly coupled



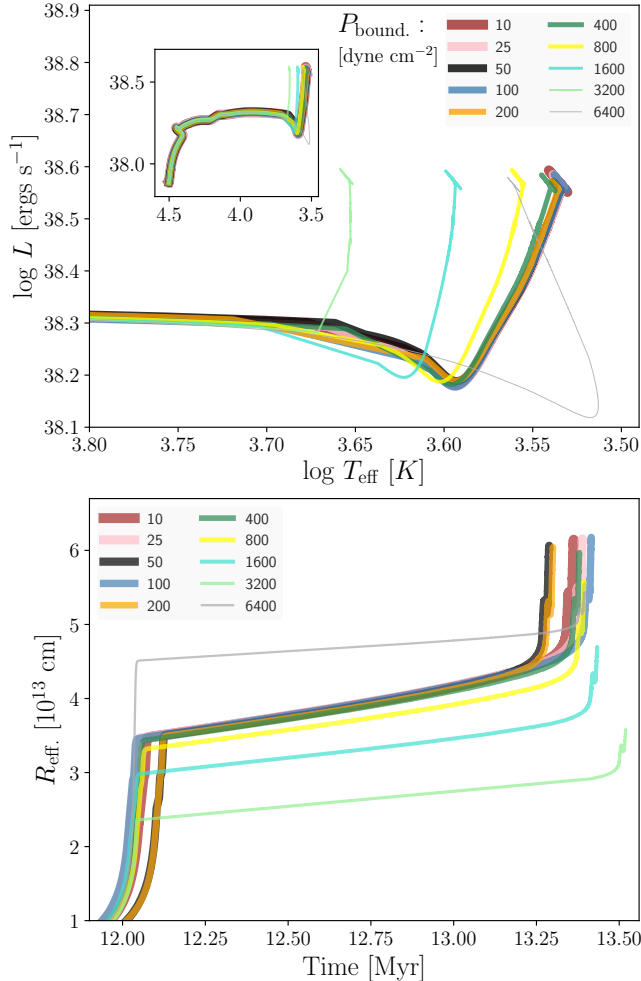


FIG. 3.— (Top panel:) The HR-diagram for variations of Model 15.00D (Table 1) in which the surface boundary pressure is varied from 10 dyne  $\text{cm}^{-2}$  to 6400 dyne  $\text{cm}^{-2}$  in roughly factor of two steps. The inset shows that the evolution is insensitive to this boundary condition until the star becomes a red supergiant. The main figure shows nearly identical results for pressures  $\lesssim 500$  dyne  $\text{cm}^{-2}$ , but significant variations for larger values. (Bottom panel:) Radius as a function of time during the final evolution of the same models. Only the last 1.4 Myr when the stars become RSGs is shown. Models with boundary pressures less than 500 dyne  $\text{cm}^{-2}$  have nearly identical radii as supergiants until very close to the end while those with bigger pressures vary. The time spent as RSG’s is similar.

in the code). Very little difference was noted in a few test cases when this maximum step was increased to  $5 \times 10^{10}$  s.

Minor changes to improve the stability of the code when transitioning to silicon quasiequilibrium and the convergence criteria were also incorporated. These had insignificant effects on the outcome, but improved code performance. Models for the main survey were all calculated on identical processors using the same version of the code and compiler so as to reduce any possible noise introduced by machine architecture (Ohio Supercomputer Center 1987).

One major goal of this work was to explore the effect of resolution on calculations of presupernova structure. The number of zones used in the main survey was typically  $4,000 \times (M_{\text{ZAMS}}/12 M_{\odot})$ . Stars more massive than

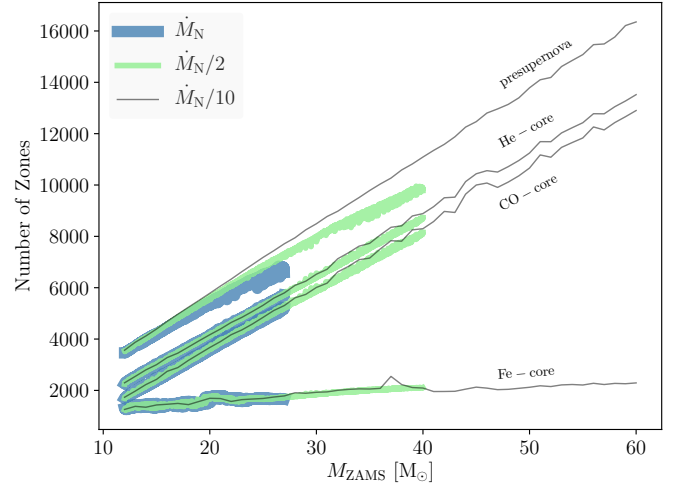


FIG. 4.— Total number of zones in the presupernova star as a function of main sequence mass for the model sets with standard mass loss rate  $\dot{M}_{\text{N}}$  (blue), with reduced rate of  $\dot{M}_{\text{N}}/2$  (green) and reduced rate of  $\dot{M}_{\text{N}}/10$  (black). In order to maintain fine resolution in stars of increasing mass, the number of shells becomes greater. The lower curves show the zoning inside the helium core, the carbon-oxygen core and iron-core. These new models retain more zones only in the iron-core alone as the earlier studies did in the whole star.

$30 M_{\odot}$  thus had over 10,000 initial mass shells. In all cases, the maximum mass zone anywhere in the star was, at all times,  $\lesssim 0.01 M_{\odot}$ , but zoning was by no means uniform. The initial zoning (Fig. 4), which continued to characterise most of the star until the presupernova stage, had much finer zoning in the helium core, down to about  $0.001 M_{\odot}$  at the stars center.

Except as noted above for hydrogen burning, the time step criteria were not varied from the previous studies. Nevertheless the finer resolution of the new runs did result in taking more time steps as smaller zones experienced mass loss or were cycled through the large density contrast at the base of the hydrogen convective shell. Abundances within a given zone convectively coupled to many other zones also required more time steps to change. The typical number of steps for a new calculation is 45,000, about twice the earlier studies  $\sim 25,000$ .

The presupernova structure and composition tables for all models from the main sets with  $\dot{M}_{\text{N}}$ ,  $\dot{M}_{\text{N}}/2$  and  $\dot{M}_{\text{N}}/10$  are available through the Harvard-Dataverse archive<sup>9</sup>.

## 4. RESULTS

### 4.1. Observable Properties

The observable properties of the new models are summarized in Fig. 5, Fig. 6, and Table 4. Final (presupernova) masses are sensitive both to the uncertain mass loss rate prescription (Nieuwenhuijzen & de Jager 1990), and to the uncertain history of the stellar radius. The results vary considerably. For lower mass stars, the spread in final mass is smaller since the star only loses a small amount of mass. For bigger stars, though, a large fraction of the hydrogen envelope may be lost. Most of the mass loss occurs during helium burning, and most of that, during the late stages when the central helium mass fraction is less than 0.5.

<sup>9</sup> <http://doi.org/10.7910/DVN/VOEXDE>

Since the luminosity does not vary greatly during helium burning, the amount of mass lost, and its uncertainty, depends mostly upon the radial history of the star -  $R^{0.8}$  in the Nieuwenhuijzen & de Jager (1990) formalism, i.e., the amount of time the helium burning star spends as a blue supergiant (BSG) or RSG. It is well known that the semi-convective mixing and overshoot mixing play a key role in determining the ratio of time spent as each (Lauterborn et al. 1971). In the present calculations, small changes in individual semiconvective mixing episodes affect the timing of the development of a deep surface convection zone, and hence the movement of the star to the red. With more semiconvection, the star spends a greater fraction of its helium burning lifetime as a BSG and hence loses less mass, ending its life with a larger hydrogen envelope still intact. RSGs have the converse behaviour. Less semiconvection, e.g., strictly Ledoux convection, favors a longer time as a RSG and thus reduces the threshold for a massive star to lose its envelope. Though the spread in Fig. 5 looks large, the uncertainty is usually a small fraction of the total mass lost. For example a  $25 M_{\odot}$  star with the standard mass loss rate might end up as a  $12$  or  $15 M_{\odot}$  star. That is it might lose  $10$  to  $13 M_{\odot}$ , a range of about 25 %. Lower mass models have a smaller variation.

The final masses for stars calculated using  $\dot{M}_N/2$ , of course, are larger. Bigger stars on the main sequence then retain more envelope by the time they die, and we were thus able to determine the core structure of more massive stars. For the most massive models considered the final hydrogen envelope mass was roughly  $4 M_{\odot}$  for the  $\dot{M}_N$  models and  $5 M_{\odot}$  for the  $\dot{M}_N/2$  models. For smaller envelope masses, the radius expanded beyond  $1.5 \times 10^{14}$  cm and became unstable, in the KEPLER code, due to recombination. In these cases, the envelope could only be retained on the star by the addition of a large, unrealistic boundary pressure that resulted in gross density inversions in the outer envelope. We suspect that this is a real instability in nature, that once the envelope mass decreases below a critical value in a very massive star and the radius extends beyond 10 AU, the remaining envelope is lost through non-steady processes (Sanyal et al. 2015, 2017). The luminosity in the hydrogen envelope is a substantial fraction of the Eddington value. This interesting possibility is deferred for a later study.

Since a larger pressure can give a smaller radius and reduced mass loss, different choices of boundary pressure can lead to significant differences in the final mass. The boundary pressure used in Müller et al. (2016), for example, several thousand dyne  $\text{cm}^{-2}$ , was larger than what we now believe reasonable and much larger than used in the present study, 50 dyne  $\text{cm}^{-2}$ . This probably accounts, at least partly, for the larger final masses found in the Müller et al. (2016) study and accounts for their ability to study higher mass stars using a single mass loss prescription.

This boundary pressure does not appreciably affect the compactness of the cores for stars of given main sequence masses, however. This is because the large spread in final star masses (Fig. 5) is not reflected in the helium core mass (§4.2) or the luminosity of the star (Fig. 6). Since the core structure, which is the main focus of this paper, is chiefly sensitive to the helium core mass and not the

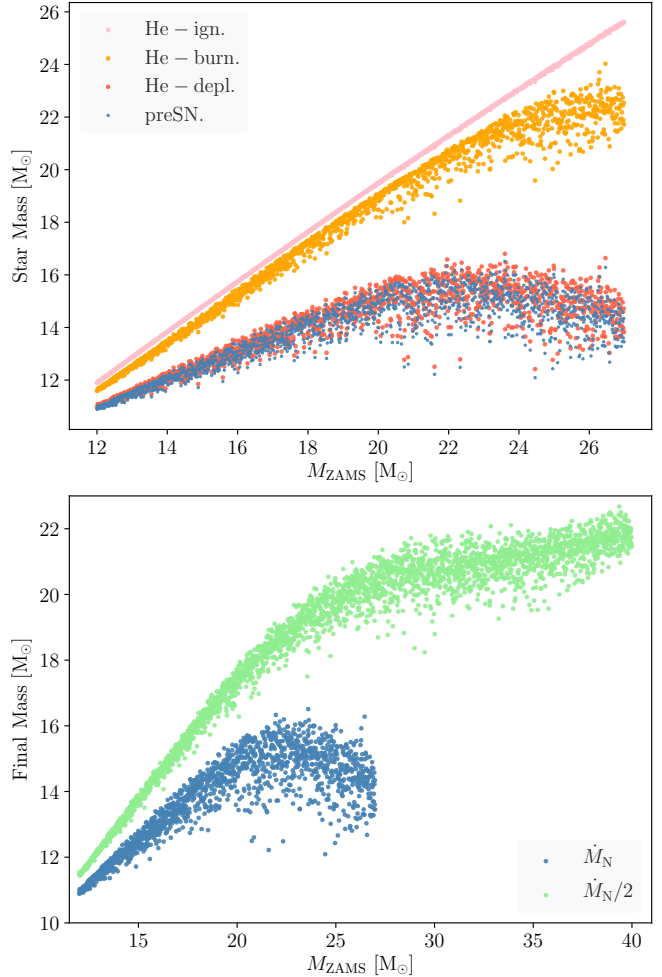


FIG. 5.— Stellar masses during helium burning and for presupernova stars. The upper panel shows results for standard mass loss ( $\dot{M}_N$ ) at helium ignition (pink) when 1 % of the helium has burned to carbon; helium burning (orange) when central helium mass fraction is 50 %; helium depletion (red) when the central helium mass fraction is 1 %; and the presupernova star (blue). The presupernova masses and helium depletion masses are almost indistinguishable. Most of the mass loss, and most of the dispersion in the presupernova mass, arises due to radius expansion after substantial helium has already burned. The lower panel shows the larger presupernova masses expected when the mass loss rate is reduced by a factor of two. Models with reduced mass loss generally have lower dispersion, but both show the dispersion increase with increasing initial mass (thus increasing amount of mass lost). The presupernova helium core masses show much less variation (see Fig. 7).

envelope mass, the spread in final masses seen in Fig. 5 does not affect our major conclusions.

Fig. 6 and Table 4 give the final luminosities and effective temperatures of our presupernova models. The luminosity of the presupernova star depends chiefly on the helium core mass and is approximately given by  $L_{\text{preSN}} \approx 5.77 \times 10^{38} (M_{\text{He}}/6M_{\odot})^{1.5}$  ergs  $\text{s}^{-1}$ . The effective temperature, essentially bounded by the Hayashi limit remains pegged at close to  $\sim 3500$  K for all presupernova stars. Thus the radius of the star increases as  $M_{\text{He}}^{0.75}$ . Except for a few presupernova stars, most RSGs will be observed during their helium burning stage where their effective temperatures will be hotter. Our calculations show a systematic  $\sim 200$  K offset between the effective temperatures at helium depletion and presupernova.

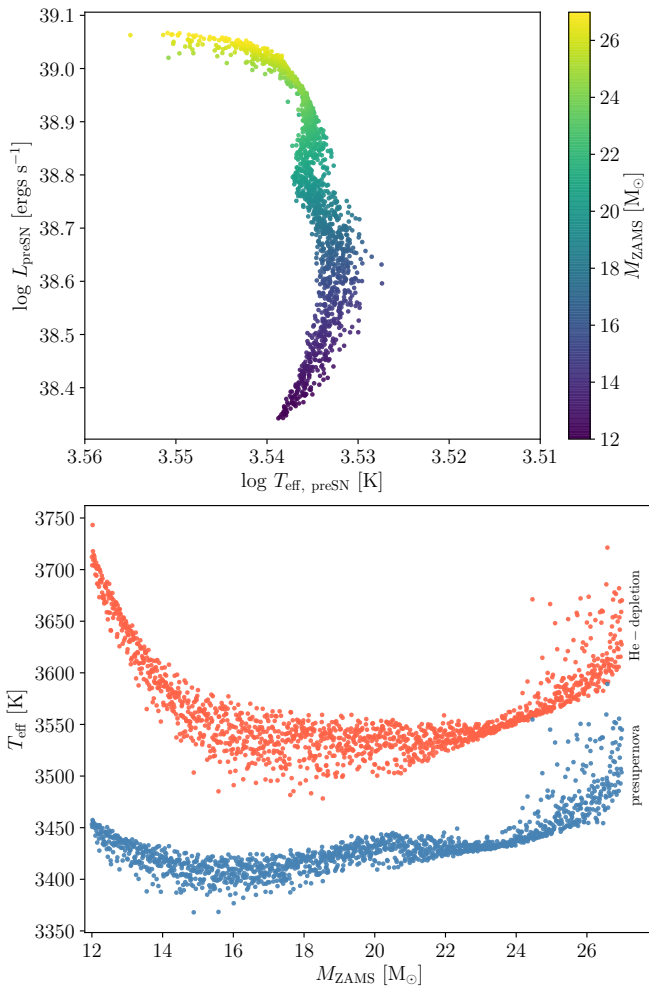


FIG. 6.— (Top panel:) Location in the HR-diagram for the presupernova stars that used the standard mass loss rate ( $\dot{M}_N$ ). (Bottom panel:)  $T_{\text{eff}}$  at helium depletion (red) and for the presupernova stars (blue). The presupernova radii vary almost linearly from  $5 \times 10^{13}$  cm to  $10 \times 10^{13}$  cm as the mass increases from 13 to 26  $M_{\odot}$ . The stars all die with a nearly constant effective temperature between 3400 and 3600 K. Observations would select RSGs prior to helium depletion, so the helium-depletion curve (red) in the lower panel is a lower bound to what is likely to be observed for  $T_{\text{eff}}$ .

nova stars. Earlier in helium burning the temperature will be even hotter and thus  $T_{\text{eff}} \approx 3,550$  K should be a lower bound to what is seen. Larger values are also expected for sub-solar metallicity and lower values for presupernova stars. These numbers are in good accord with measurements of the hottest RSGs (Davies et al. 2013; Levesque et al. 2005).

#### 4.2. Core Masses

Fig. 7 shows the helium, carbon-oxygen (CO), and iron-core masses for all our presupernova models with  $\dot{M}_N$  and  $\dot{M}_N/2$ . The dispersion in helium and CO core masses for a given main sequence mass is small, much less than the hydrogen envelope masses inferred in Fig. 5. This implies that the helium and CO core masses are only slightly affected by the assumed mass loss rate and are probably not very sensitive to metallicity. The helium core mass as a function of main sequence mass is approximately  $M_{\text{He}} \approx 6.46 (M_{ZAMS}/20)^{1.27}$  which can

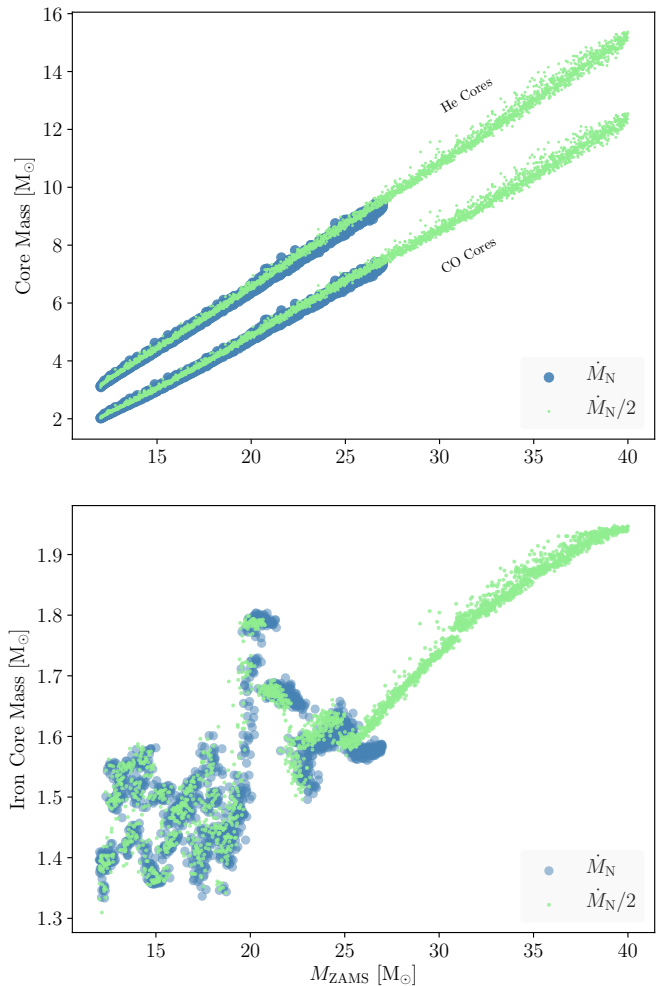


FIG. 7.— Helium core, CO core, and Fe core masses for all presupernova stars from sets with  $\dot{M}_N$  and  $\dot{M}_N/2$ . Despite significant variations in mass loss (Fig. 5), the final helium and carbon-oxygen cores are well determined by the star’s initial mass and a standard choice of stellar physics. Note multiple branches for the iron core mass below 19  $M_{\odot}$ .

be combined with the previous relation in §4.1 to give  $L_{\text{preSN}} \approx 6.5 \times 10^{38} (M_{ZAMS}/20 M_{\odot})^{1.92}$  ergs  $\text{s}^{-1}$ . Since presupernova core compactness is chiefly a function of helium core mass (Sukhbold & Woosley 2014), these results suggest a near universal dependence of presupernova core structure on initial mass, provided mass loss does not remove the entire hydrogen envelope.

Iron core masses increase, on the average with increasing stellar mass reaching maximum of about 2.0  $M_{\odot}$  for the most massive stars studied ( $> 40 M_{\odot}$ ). Still larger iron cores, up to about 2.5  $M_{\odot}$  characterize more massive stars in the pulsational-pair instability range (70 - 140  $M_{\odot}$ ; Woosley 2017). For stars below 23  $M_{\odot}$ , the iron core mass is markedly multi-valued for stars with nearly the same initial mass. This reflects the operation of multiple shells of carbon and oxygen burning as will be discussed further in §5. The two major branches of iron core masses below 20  $M_{\odot}$ , which are most of the stars that leave neutron star remnants might result in bimodality in the neutron star mass function.

#### 4.3. Core Structure

TABLE 4  
 PROPERTIES OF THREE MAIN MODEL SETS

$M_{\text{ZAMS}}$ [ $M_{\odot}$ ]	$M_{\text{preSN}}$ [ $M_{\odot}$ ]	$M_{\text{He}}$ [ $M_{\odot}$ ]	$M_{\text{CO}}$ [ $M_{\odot}$ ]	$\log L_{\text{preSN}}$ [ergs s $^{-1}$ ]	$T_{\text{eff, preSN}}$ [K]	$T_{\text{eff, He dep}}$ [K]	$R_{\text{preSN}}$ [ $10^{13}$ cm]
$\dot{M}_{\text{N}}$ (binned by 1 $M_{\odot}$ )							
12	11.19	3.35	2.20	38.39	3440	3670	4.97
13	11.72	3.79	2.53	38.47	3420	3610	5.49
14	12.22	4.20	2.85	38.54	3410	3570	5.97
15	12.73	4.61	3.19	38.60	3405	3545	6.41
16	13.23	5.01	3.53	38.65	3405	3535	6.80
17	13.74	5.42	3.87	38.69	3410	3535	7.15
18	14.12	5.84	4.24	38.73	3420	3530	7.45
19	14.60	6.24	4.60	38.77	3425	3530	7.72
20	14.87	6.66	4.98	38.81	3430	3535	8.07
21	14.97	7.09	5.35	38.85	3430	3535	8.51
22	15.09	7.49	5.71	38.90	3430	3540	8.95
23	15.11	7.90	6.05	38.94	3435	3550	9.36
24	14.72	8.34	6.44	38.98	3450	3565	9.73
25	14.49	8.75	6.80	39.01	3470	3590	10.01
26	14.27	9.15	7.15	39.04	3500	3620	10.20
$\dot{M}_{\text{N}}/2$ (binned by 1 $M_{\odot}$ )							
12	11.82	3.39	2.22	38.40	3460	3685	4.95
13	12.59	3.82	2.55	38.47	3450	3630	5.44
14	13.35	4.24	2.88	38.54	3440	3595	5.90
15	14.12	4.65	3.22	38.60	3440	3580	6.31
16	14.87	5.07	3.58	38.65	3440	3570	6.71
17	15.62	5.49	3.93	38.70	3450	3565	7.04
18	16.37	5.91	4.30	38.74	3460	3565	7.32
19	17.01	6.36	4.69	38.78	3465	3560	7.65
20	17.66	6.79	5.08	38.82	3465	3560	8.04
21	18.27	7.22	5.45	38.87	3460	3560	8.49
22	18.69	7.67	5.85	38.92	3455	3560	9.00
23	19.25	8.07	6.20	38.96	3455	3565	9.42
24	19.58	8.52	6.59	39.00	3455	3565	9.86
25	19.95	8.94	6.94	39.03	3455	3570	10.23
26	20.14	9.38	7.31	39.06	3460	3575	10.60
27	20.36	9.80	7.67	39.09	3465	3585	10.92
28	20.66	10.19	7.99	39.11	3470	3590	11.19
29	20.61	10.65	8.38	39.14	3480	3600	11.50
30	20.72	11.08	8.73	39.17	3495	3610	11.75
31	20.83	11.49	9.10	39.19	3510	3625	11.97
32	20.85	11.95	9.48	39.21	3525	3640	12.18
33	20.98	12.37	9.86	39.23	3540	3655	12.37
34	21.03	12.85	10.27	39.26	3560	3675	12.55
35	21.08	13.33	10.70	39.28	3580	3690	12.74
36	21.36	13.69	11.01	39.29	3590	3705	12.86
37	21.40	14.18	11.46	39.31	3610	3725	12.99
38	21.63	14.56	11.80	39.33	3625	3735	13.15
39	21.80	14.98	12.18	39.34	3635	3750	13.29
$\dot{M}_{\text{N}}/10$ (not binned)							
12	11.88	3.21	2.09	38.36	3480	3725	4.69
15	14.76	4.46	3.07	38.58	3465	3615	6.05
20	19.48	6.66	4.96	38.81	3500	3590	7.76
25	24.00	8.86	6.89	39.02	3495	3605	9.88
30	27.75	11.39	8.95	39.17	3510	3615	11.73
35	31.55	13.89	11.05	39.29	3535	3625	13.17
40	35.25	16.23	13.19	39.37	3575	3660	14.23
45	36.65	21.41	18.22	39.53	3610	3650	16.73
50	41.40	21.21	17.87	39.52	3635	3710	16.28
55	44.27	23.73	20.20	39.58	3655	3715	17.26
60	47.31	25.64	22.00	39.62	3680	3740	17.79

NOTE. — All quantities are measured at the presupernova stage, except  $T_{\text{eff, He dep}}$ , which was measured when the helium mass fraction in the core was depleted to 1 %. All  $T_{\text{eff}}$  values were rounded to multiples of 5.

### 4.3.1. Measures of “Explodability”

Early theoretical studies of supernovae noted a strong correlation of a rapidly declining density outside the iron core with the degree of difficulty encountered in trying to explode the star using the neutrino energy transport (e.g., Burrows & Lattimer 1987; Fryer 1999). O’Connor & Ott (2011) introduced a simple, single parameter measure of this density decline called the “compactness parameter”:

$$\xi_M = \frac{M/M_\odot}{R(M_{\text{bary}} = M)/1000 \text{ km}} \Big|_{t_{\text{bounce}}}, \quad (3)$$

where  $R(M_{\text{bary}} = M)$  is the radius of the Lagrangian mass shell enclosing mass  $M$  in the presupernova star. The fiducial mass is often chosen as the innermost  $2.5 M_\odot$  so that for a wide range of initial masses it not only encloses the iron-core but samples enough of the overlying shell material around it. Though the parameter is defined to be evaluated at the time of bounce, it is more often measured at the time of presupernova (when the collapse begins), since the systematics are insensitive to slightly different fiducial choices (Sukhbold & Woosley 2014). Subsequent studies by Ugliano et al. (2012), O’Connor & Ott (2013), and Sukhbold et al. (2016) showed strong correlation between the ease with which model stars exploded and the  $\xi$  parameter, in the sense that stars with small  $\xi$ , i.e., steep density gradients outside the iron core were easier to explode using a standard, albeit approximate, set of supernova physics. Although this is a useful starting point, a single parameter conveys limited information about the structure of the core and more physics-based representations followed.

In particular, Ertl et al. (2016) suggested an alternative two-parameter characterisation based upon  $M_4$ , the mass coordinate, in solar masses, where the entropy per baryon reaches  $4.0 k_B$ , and the radial gradient,  $\mu_4$ , of the density at that point. In practice,  $\mu_4$ , was obtained by evaluating the change in mass over the change in radius between several mass shells separated by  $0.3 M_\odot$  in the vicinity of  $M_4$ , i.e.,

$$\mu_4 = \frac{dm/M_\odot}{dr/1000 \text{ km}} \quad (4)$$

where  $dm = 0.3 M_\odot$ . Smaller values of  $\mu_4$  thus imply steeper density gradients (less change in enclosed mass when the radius changes). The quantity  $M_4$  has long been used to locate the steep density decline often associated with a strong oxygen-burning shell in the presupernova star (e.g., Woosley & Heger 2007). Where the entropy per baryon abruptly rises at nearly constant temperature, the density declines. When the core collapses, the arrival at the neutrinosphere of lower density matter reduces the “ram pressure” and facilitates the launch of an outgoing shock. Besides its location, it is helpful to characterise the rate of the density change, which is the role played by  $\mu_4$ .

It is reasonable that higher neutrino luminosities and smaller accretion rates on the proto-neutron star should favor explosion. Ertl et al. (2016) made the case that  $\mu_4$ , multiplied by its radius (i.e., the radius at which  $M_4$  is found) and divided by a collapse time scale, is a surrogate for the accretion rate at the time of explosion. The product  $\mu_4 M_4$  is similarly a surrogate for the accretion

luminosity. This assumes, as the models suggest, that the radius where the neutrino luminosity is generated does not vary greatly with mass. Explosion is thus favored by small  $\mu_4$  (accretion rate) and large  $\mu_4 M_4$  (luminosity). Ertl et al. (2016) determined a simple condition expressed as a straight line

$$\mu_4 = k_1(\mu_4 M_4) + k_2 \quad (5)$$

such that models that lay below the line (lower  $\mu_4$ ) were more likely to explode than those above. The values  $k_1$  and  $k_2$  were determined from several large scale simulations and leading models for SN 1987A. For one representative set,  $k_1 = 0.194 (M_\odot)^{-1}$  and  $k_2 = 0.058$  (“N20” model in their Table 2).

More recently, Müller et al. (2016) adopted a different approach using a semi-analytic model for the explosion based upon presupernova properties. By using a fuller description of the presupernova star than afforded by just one or two parameters, they were able to approximately estimate not only the success or failure of the explosion, but also the explosion energy, ejected nickel mass, and compact remnant mass. This approach does not include, in its present form, several important pieces of explosions physics, such as proto-neutron star cooling, self-consistent fallback and explosive nuclear burning, and thus it is not as powerful as the parameterised simulations such as Sukhbold et al. (2016). Its main power lies in its ability to rapidly calculate general trends in explosion properties that depend on presupernova structure. Their approach uses five physically motivated parameters to determine the outcome. Here we analyze our new presupernova models using their standard values -  $\beta_{\text{expl}} = 4$ ,  $\zeta = 0.7$ ,  $\alpha_{\text{out}} = 0.5$ ,  $\alpha_{\text{turb}} = 1.18$ , and  $\tau_{1.5} = 1.2$  (see their Table 1). For the definitions of these parameters and further technical details see Müller et al. (2016).

### 4.3.2. Results for the Compactness Parameter

Fig. 8 shows the compactness parameter,  $\xi_{2.5}$ , i.e.,  $\xi$  for our three model sets measured at a fiducial mass of  $2.5 M_\odot$  at the time the presupernova collapse speed reaches  $900 \text{ km s}^{-1}$ . One notable feature seen in Sukhbold & Woosley (2014) is the relatively large “scatter” of compactness parameter between 18 and  $22 M_\odot$ , which are now shifted to roughly 14 and  $19 M_\odot$  (Panel a) with updated neutrino-losses (§2). As has long been noted (e.g. Timmes et al. 1996),  $\sim 20 M_\odot$  marks the transition region between exoergic convective central carbon burning, at lower masses, to endoergic radiative burning at higher ones. That is, at high mass the energy produced by carbon fusion does not exceed neutrino losses in the star’s center and it proceeds from helium depletion to oxygen ignition on a short Kelvin-Helmholtz time scale. As a result subsequent burning especially in shells, where the net energy generation is positive, proceeds differently. The carbon convective shells move inwards (with increasing initial mass) up until this transition point and are weaker and more in number (Barkat 1994).

Quite noticeable in the new results and also in the prior work of Müller et al. (2016) are concentrations of points in the compactness parameter plot, which were not clearly seen in our earlier studies due to much coarser increments in mass-space. Points are not randomly scattered between some local maximum and minimum value. Note for example, the existence of two, and possibly three



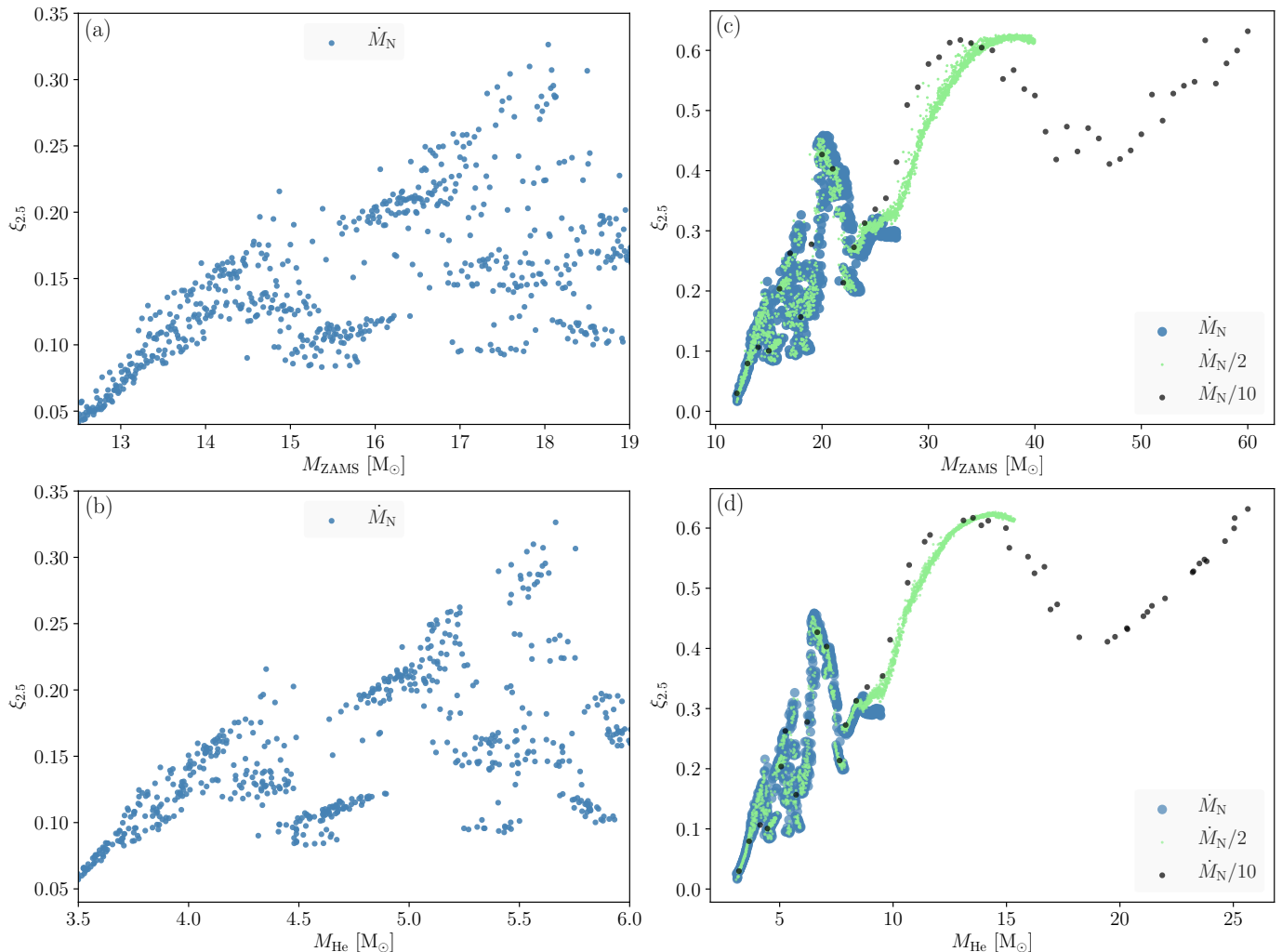


FIG. 8.— (a): The compactness parameter for a fiducial mass of  $2.5 M_{\odot}$  evaluated at the presupernova stage shown for models below  $< 19 M_{\odot}$  as a function of initial mass for the  $\dot{M}_{\text{N}}$  set. Even where rapid variations occur, the scatter is not wholly random. Points tend to concentrate in one of several solutions. (b): Same points as in (a) now shown as a function of helium core mass. The branching solutions are more clearly seen. The range of  $\xi_{2.5}$  seen in this mass range includes stars that might explode or implode, and thus both outcomes are possible for stars with nearly identical initial mass. (c): Compactness shown for all three values of mass loss. Slight shifts between the sets are due to the growth of the helium core by hydrogen shell burning, resulting in a slightly larger compactness for the models with reduced mass loss. (d): same points as in (c) are now shown as a function of helium core mass. Much of the shift seen in (c) is gone since the helium core mass is a chief determinant of the core structure.

discrete solutions for helium core masses near  $4.8 M_{\odot}$  (Panel b). Multiple branches also exist at other masses but with less clarity. For a helium core mass of  $5.6 M_{\odot}$ , the compactness parameter for stars with nearly identical masses varies by a factor of three, from  $\xi_{2.5} = 0.1$  to  $0.3$ . Such a large variation spans the range of stars that might explode or collapse to black holes, and suggests that both outcomes are possible for relatively low mass stars of almost the same initial mass.

When all three new sets are plotted as a function of initial mass (Panel c), the models with lower mass loss rate are slightly shifted with respect to models with higher mass loss rate. The shifts are hardly noticeable at lower initial mass ( $< 20 M_{\odot}$ ), but they grow with increasing mass and for our most massive models the  $\dot{M}_{\text{N}}/10$  set is shifted by a few  $M_{\odot}$  with respect to  $\dot{M}_{\text{N}}/2$  set. The primary reason for this shift is that for a given initial mass, models with lower mass loss rate attain slightly larger He-cores and slightly different compositions. There is also

a general underlying scatter, similar to the one of total star mass shown in Fig. 5, some of which result from the slight change of He core mass due to semiconvective effects discussed in §4.1.

Panel (d) of Fig. 8 shows the compactness as a function of He-core mass for all of our models. Since the initial mass scales cleanly with He-core mass (Fig. 7), the structure of the curve stays nearly identical, however, the above mentioned shifts and scatters are mostly gone. The He-core mass and within it, the CO-core mass, are the chief determinants of core structure, not the final supernova mass which includes the hydrogen envelope. Uncertainties in mass loss rates are thus not particularly relevant to the compactness, except for determining the main sequence mass above which the entire envelope is lost.

As was noted by O'Connor & Ott (2011) and studied many times since, the compactness plotted against mass is non-monotonic and highly structured with two distinct peaks in the vicinity of  $21$  and  $35 M_{\odot}$  (Sukhbold

& Woosley 2014). A shallow dip, occurs near  $50 M_{\odot}$  followed by a slow rise at still higher masses (Sukhbold & Woosley 2014) until finally the pulsational-pair domain is reached near  $70 M_{\odot}$ . As discussed in Sukhbold & Woosley (2014) and Sukhbold (2016), this structure is crafted out of an overall gradually rising curve by the operation of an advanced stage shell burning episode of one fuel modulating the core burning episode of the next fuel. In particular, the structure near the first peak is primarily driven by the effect of shell carbon burning on core oxygen burning, while the structure near the second peak is driven by the effect of shell oxygen burning on core silicon burning. At very high mass, oxygen burning ultimately ignites a strong shell outside of  $2.5 M_{\odot}$ , and therefore the compactness stays high.

Fig. 9 compares the new results with those of Sukhbold & Woosley (2014) and Müller et al. (2016), and illustrates these points. Most notable is a shift of the new models above  $\sim 14 M_{\odot}$  downwards in mass by about 2 to  $3 M_{\odot}$  compared with Sukhbold & Woosley (2014). This is a consequence of fixing the bug in the neutrino losses as discussed in §2, and not due to differing resolution. Models below  $14 M_{\odot}$  are affected very little, but the more massive stars change appreciably. The region of variability which was between 18 and  $22 M_{\odot}$  in Sukhbold & Woosley (2014) is now shifted down to 14 to  $19 M_{\odot}$ . If anything that variability, is now greater with the finer resolution, perhaps due to the larger number of models surveyed.

Indeed, the comparison with Müller et al. (2016), who used the corrected neutrino loss rate and sampled many more models is excellent, both in the location of structures and the range of  $\xi_{2.5}$  within those structures. This agreement persists despite the use of 4 to 10 times more mass shells in each of the new models and a radical decrease in the surface boundary pressure. The latter affected the mass lost by the star, but not appreciably the helium core masses. There is no reason to believe that still finer zoning, smaller time steps, or a different reaction network will greatly alter these results, unless the code physics itself (reaction rates, semiconvection, rotation, etc.) is changed. The studies of Müller et al. (2016) and the present work are mutually confirming.

#### 4.3.3. New Results and the Ertl Parametrization

An important subsidiary question is whether  $\xi_{2.5}$  is really the best measure for presupernova core structure. Might some of the variability seen in Fig. 8 be simply because of the choice of a single arbitrary point in the star to sample its structure? Perhaps other parametrizations might give less variability and more reliable predictions? In particular,  $\xi_{2.5}$  is sensitive to recent shell activity in the vicinity of  $2.5 M_{\odot}$  that might not always describe well what went on deeper inside.

The Ertl parametrization of our results is given in Fig. 10. As previously discussed (§4.3), points beneath the dashed line represent models that are more likely to explode in a simple neutrino transport scheme. Multi-valued solutions are clearly seen, especially for stars with  $\mu_4 M_4$  less than 0.25. In some ranges, the difference between solutions is enough to significantly affect the probable outcome of the explosion. Stars with  $\mu_4 M_4$  less than 0.25 typically have masses less than  $20 M_{\odot}$ . For more massive stars, and, in particular, for  $\mu_4 M_4$  greater

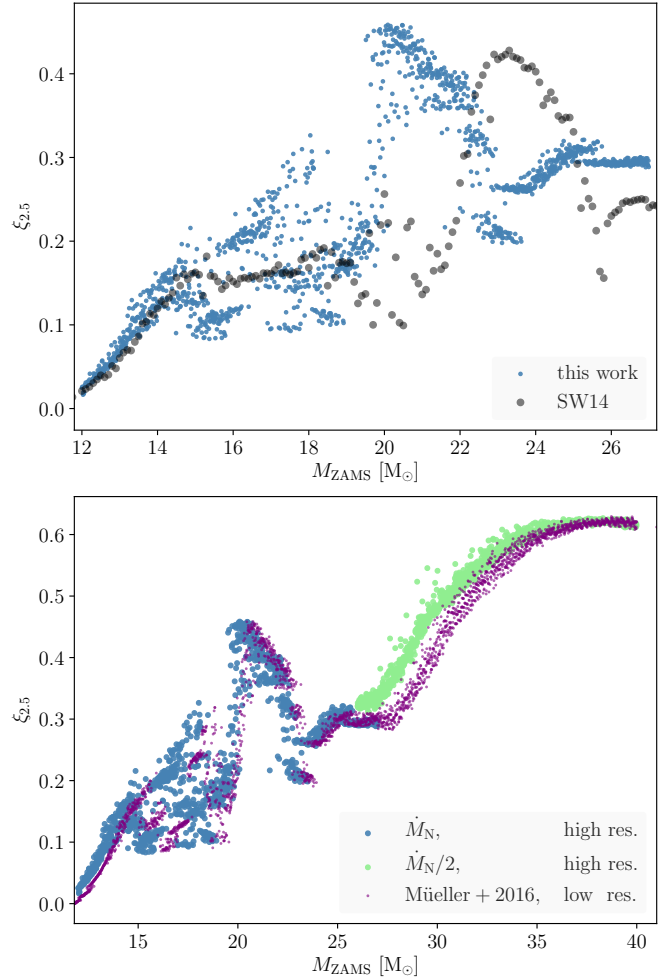


FIG. 9.— Presupernova compactness compared with previous results for solar metallicity stars obtained by Sukhbold & Woosley (2014) (top frame) and Müller et al. (2016) (bottom frame). The new models differ little from Sukhbold & Woosley (2014) below  $14 M_{\odot}$ , but the peak in compactness formerly at  $23 M_{\odot}$  is shifted downwards to about  $20.5 M_{\odot}$ . The “noise” noted by Sukhbold & Woosley (2014) from  $17$  to  $22 M_{\odot}$  is also shifted downwards to  $14$  to  $19 M_{\odot}$  and now with finely incremented models it shows several concentrations of points suggestive of a multi-valued solution. The lower panel shows comparison with the work of Müller et al. (2016). Since the  $\dot{M}_N$  and  $\dot{M}_N/2$  sets are nearly identical at lower mass (Fig. 8), for clarity, we have plotted  $\dot{M}_N$  set for lower mass and  $\dot{M}_N/2$  set for higher mass. The agreement between these models with those from Müller et al. (2016) is substantial, even though the current survey uses more models, carried more zones and timesteps per model. Reducing the mass loss (see text) shifts the results towards slightly lower main sequence mass.

than 0.25, explosion seems quite unlikely. Reasons for the multi-valued solution are discussed in §5.

Also striking is the much tighter clustering of points in the Ertl representation of our new models (Fig. 10) in contrast with an equivalent plot of “compactness” (Fig. 8). The results are less noisy and also show less overall variability. This is due to the obvious correlation between two Ertl parameters on one hand, but it also presumably reflects the better representation of core structure by a two-parameter, physics-based representation than a single parameter anchored to a single point in the core. It also suggests that much of the “noise” in Fig. 8, especially for initial masses  $14 - 19 M_{\odot}$  may not



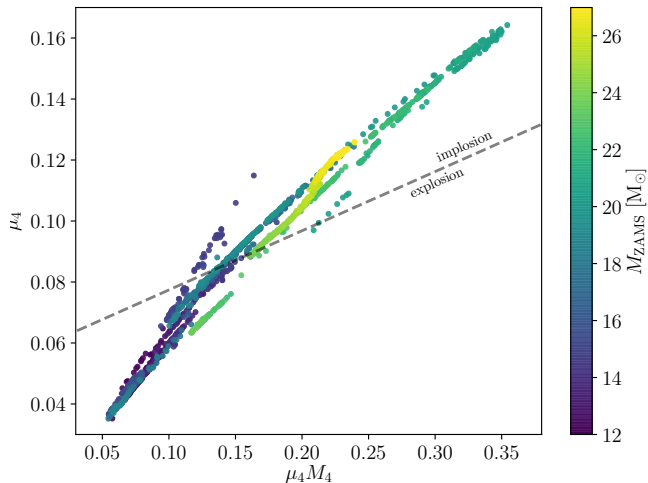


FIG. 10.— “Explodability” according to sample “engine” model from Ertl et al. (2016). The Ertl parameters,  $\mu_4$  and  $\mu_4 M_4$ , are shown for the new models with standard mass loss rates. See text for definitions. Points above the dashed line are more likely to explode than those below. Multiple solutions are clearly visible for  $\mu_4 M_4$  below  $0.25 (M_\odot)^{-1}$ . The scatter in this figure is a lot less than Fig. 9.

be so much a consequence of “non-convergence” of the models, but as a poor representation of the results.

### 5. INTERPRETATION

Why is the core structure of presupernova stars non-monotonic and multi-valued for some ranges of mass? The short answer is that the advanced stage evolution of massive stars involves two to three carbon burning shells (plus central core burning for models below  $\sim 19 M_\odot$ ) and one or two oxygen shells (plus core burning). Combinations of these shells lead to variable outcomes, but not a continuum of all possibilities, because shells have finite sizes and their number is an integer. The transitions are abrupt and small changes upstream in the strength or extent of one or more shells can send a star down one path or another. This is especially true for stars below  $19 M_\odot$  where there are more carbon burning shells.

Globally,  $\xi_{2.5}$ ,  $\mu_4$ , and  $M_4$  all increase gradually with mass. Higher mass stars have greater entropy in their middles and are less degenerate in their final stages. Greater degeneracy leads to an increased central concentration of the mass and “core convergence.” For lighter stars, the presupernova structure resembles more a white dwarf embedded in a low density envelope, where the density declines rapidly at the edge of the central “white dwarf”. This effect is clearly at work in the lightest stars surveyed. Below  $13 M_\odot$ , compactness defined at a mass of  $2.5 M_\odot$  has little meaning as a measure of explodability, since the fiducial point is not even inside of the helium burning shell. For stars in this mass range, the helium burning shell always lies outside  $2 \times 10^9$  cm, thus guaranteeing a small compactness parameter. For a  $10 M_\odot$  presupernova star,  $2.5 M_\odot$  is even outside the helium core and in the hydrogen envelope. For all parametrizations of core structure considered in this paper, these light stars will always explode and need no further discussion here.

Degeneracy remains an important consideration though, even for the larger stars. A  $12 M_\odot$  presupernova

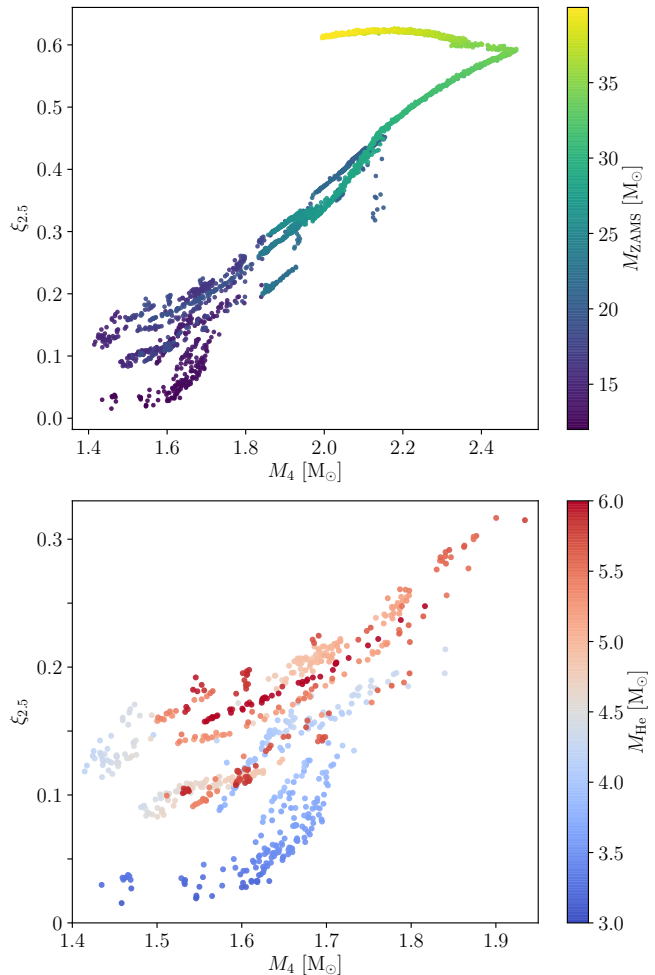


FIG. 11.— Compactness enclosing innermost  $2.5 M_\odot$  at the time of presupernova for  $\dot{M}_N/2$  and  $\dot{M}_N/10$  set of models are plotted as a function of  $M_4$ , the Lagrangian coordinate of the first mass shell where the entropy per baryon exceeds  $4.0 k_B$ . For lower mass models three major branches are clearly apparent below  $M_4 \approx 1.75 M_\odot$ . The lower panel shows a zoomed in version of the top panel, characterizing models with  $M_{ZAMS} < 20 M_\odot$ , and with color contours denoting their corresponding helium core masses.

star has a core that is degenerate (degeneracy parameter  $\eta \equiv \mu/kT > 0$ ) out to  $1.46 M_\odot$ . For  $30 M_\odot$ , degeneracy extends out to  $1.87 M_\odot$ . Even for  $100 M_\odot$ , the iron core is degenerate out to  $2.1 M_\odot$ . Most of the increase in degeneracy occurs between carbon depletion and oxygen depletion in the core when the core is efficiently cooled by the neutrinos (Sukhbold & Woosley 2014). Degeneracy affects the core structure making the (thermally adjusted) Chandrasekhar mass relevant for all stars that are likely to explode as common supernovae. On the other hand, the shells outside what will be the iron core in the presupernova star, and in particular the carbon and oxygen burning shells, are always non-degenerate. Strong burning thus leads to expansion that affects both  $\xi_{2.5}$  and  $\mu_4$ .

The upper panel of Fig. 11 shows a generally strong correlation among the compactness parameter,  $\xi_{2.5}$ , and  $M_4$ , except at very high and low masses. A correlation is expected since a sharp density decline close to the iron core requires a large radius to enclose  $2.5 M_\odot$ , thus small  $\xi_{2.5}$ . The sharp density decline implies a deeper location

where the entropy per baryon exceeds  $4.0 k_B$  and thus a smaller  $M_4$  and a steeper mass gradient at that point as well. The reversal of the plot for the most massive models is a consequence of both the increasing central entropy and the outward migration of the first oxygen shell. This migration causes a non-monotonic dependence on mass for both  $M_4$  and  $\xi_{2.5}$  as shown in Fig. 8, but  $M_4$  starts to decline at a slightly lower initial mass due to increasing entropy. Therefore when the location of  $M_4$  recedes from  $\sim 2.5$  to  $2 M_\odot$ , the  $\xi$  stays roughly constant, and results in the reversal near  $\sim 35 M_\odot$ .

The lower panel of Fig. 11 shows the behavior of compactness and  $M_4$  for stars lighter than about  $20 M_\odot$  is clearly multi-valued. Three distinct branches are apparent for the lighter stars. There is no reason to believe that more dense grid of calculations would randomly fill out the spaces between the branches.

Fig. 12 delves deeper into this correlation between compactness and  $M_4$  and helps to understand why both are multi-valued relations of mass for moderate mass stars ( $13 < M_{ZAMS} < 19 M_\odot$ ). The first panel shows  $M_4$  in the presupernova star as a function of helium core mass. A cleaner pattern results from using the helium core mass instead of the main sequence mass since it eliminates the variations due to envelope mass loss (Fig. 5). As the figure shows,  $M_4$  is usually pegged to the “oxygen shell”, by which we mean the location, in the presupernova star, where the energy generation from oxygen fusion (excluding neutrino losses) is a maximum. This is frequently, though not always interior to the boundary of the “silicon core”, inside of which the silicon mass fraction is greater than the oxygen fraction. Though one might naively assume that the oxygen burning shell is at the edge of the silicon core, this is not generally true. There are often gradients on the silicon to oxygen ratio left behind by receding convection or radiative burning. In these cases, the oxygen shell lies inside the silicon core. On the other extreme, in some stars the oxygen shell can be so active as to merge with the carbon and neon burning shells producing one large convective shell where all three are burning vigorously and the silicon core and oxygen shell are coincident. When this occurs, the compactness is usually small (Fig. 16 of Sukhbold & Woosley 2014). Many of the red points in the top panel of Fig. 12 are of this sort.

It is not surprising that the oxygen burning shell, the strongest burning shell during the late stages of stellar evolution, is usually the location of a jump in entropy. The oxygen fusion rate is very temperature sensitive, so oxygen burns at a nearly constant temperature. The overlying star expands, decreasing the local density and thus increasing the entropy. The quantity  $\mu_4$  in the Ertl parametrization is a measure of the strength of this burning.

The middle panel of Fig. 12 shows that the behavior of  $\xi_{2.5}$  in this same mass range (equivalent to Panel b of Fig. 8) correlates reasonably well with that of  $M_4$ , including, approximately, the location and extent of clusters of solutions. Within a cluster, there is usually a quasi-linear relation with a well-defined slope. A larger value of  $M_4$  implies a larger value of  $\xi_{2.5}$ . The farther out in the star the strong burning shell, the less centrally concentrated is its density. This correlation is not perfect though. Sometimes long lines in the  $M_4$  plot, e.g. the long string

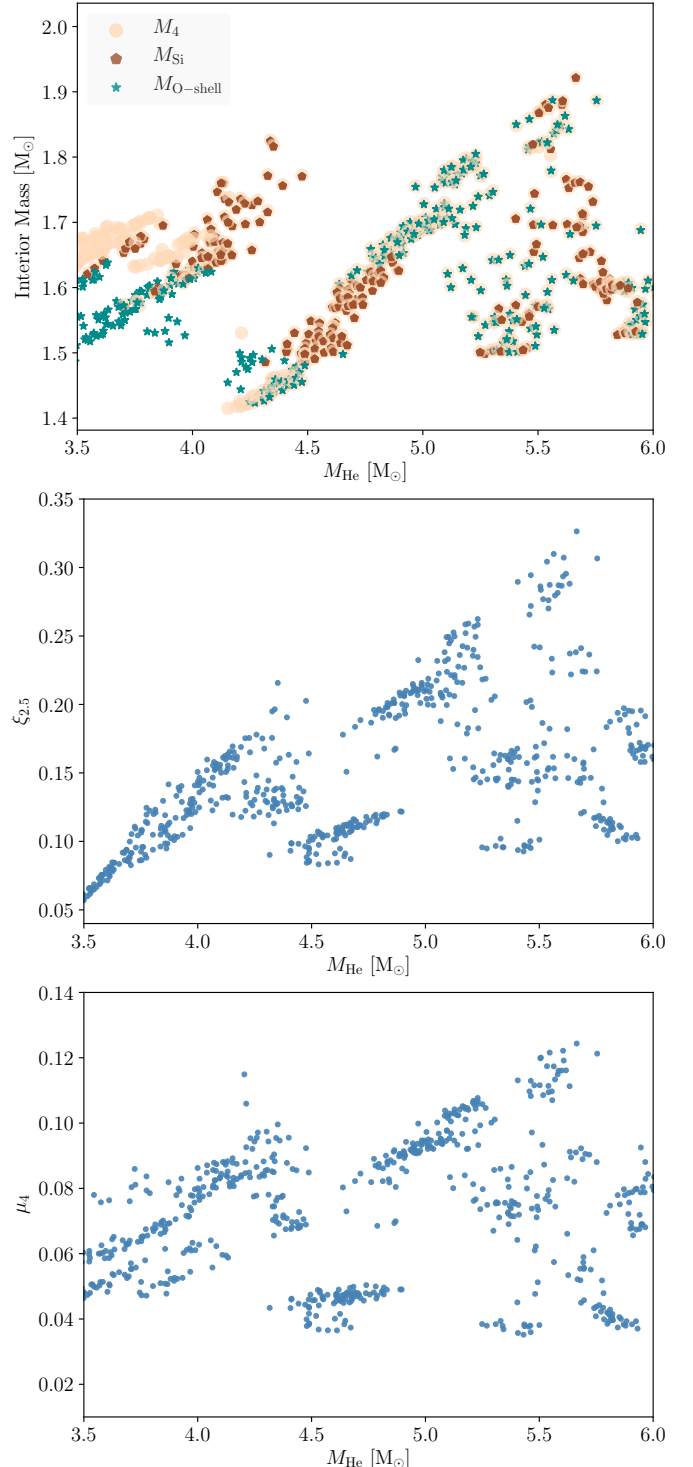


FIG. 12.— (Top:)  $M_4$  vs Helium core mass for presupernova stars with main sequence masses between 13 and  $19 M_\odot$ . Light pink points which usually underly green stars or red pentagon points indicate  $M_4$ . Green stars mark the location of the most active oxygen burning zone and red pentagons are where the silicon mass fraction first exceeds the oxygen mass fraction, going inward. For clarity, red and green points not closely affiliated to a  $M_4$  within  $0.01 M_\odot$  have not been plotted. Usually the  $M_4$  point is found at or near the maximum oxygen burning zone. Several clusters of points sometimes lying in nearly straight lines are apparent. (Middle:) The compactness parameter,  $\xi_{2.5}$  plotted for the same helium cores, equivalent to Panel b of Fig. 8. Note also a clustering of points here and a high degree of correlation with  $M_4$  in the top panel. (Bottom:)  $\mu_4$  as a function of helium core mass. Note the almost completely congruent pattern with  $\xi_{2.5}$ , since both measure the most active burning shell at the time of presupernova.

of points from  $M_{\text{He}} = 4.1 M_{\odot}$  to  $5.2 M_{\odot}$ , break into several segments with different  $\xi_{2.5}$ . This is partly due to the arbitrary pinning of  $\xi_{2.5}$  to a single mass shell, but also because specifying  $M_4$  alone does not measure the strength of the burning there.

Instead, as might be expected, the bottom panel of Fig. 12 shows that  $\xi_{2.5}$  correlates better with  $\mu_4$ , the mass gradient at  $M_4$ . This correlation is very strong since both quantities are sensitive to the strength of the most active burning shell in the last days of the star’s life. Why though are  $M_4$  and  $\mu_4$  not randomly scattered between their extrema? Why the patterns? The first panel of Fig. 12 suggests a reason.  $M_4$  traces the location of the strongest oxygen burning shell. Oxygen burns there because it is at the deepest location that has not already depleted oxygen by prior shell burning. That location is, in turn, set by the extent of oxygen burning shell(s) during the previous evolution, which in turn depends upon the entropy structure set up during carbon shell burning.

Sukhbold & Woosley (2014) pointed out this correlation between the core compactness and the extent of the first oxygen burning convective shell (their Fig. 14). Fig. 13 shows a related quantity for the new model set. The figure shows the mass of the “silicon core”, the mass interior to which oxygen has burned out, at the time silicon burning ignites in the star’s center. Here a specific central temperature,  $3.0 \times 10^9$  K, was chosen in order to make the plot, but the conditions here reflect what the oxygen burning shell (or shells) have accomplished prior to silicon ignition. Visual inspection of the convective history of these 700 models shows that the silicon core mass at silicon ignition is very nearly equal to the maximum extent of the second convective oxygen burning shell for stars below  $\sim 14.6 M_{\odot}$  (helium core mass  $4.2 M_{\odot}$ ) and of the first oxygen convective shell for more massive stars up to at least  $20 M_{\odot}$ . In this plot, we see the clearest evidence yet for regular, but non-monotonic and occasionally multi-valued behavior. Two helium cores of very nearly  $4.2 M_{\odot}$  can give rise to presupernova cores with structures in one of two well-defined states. Slight shifts in mass, composition, or even numerical approach (including zoning) can send the star one way or another.

Further analysis of the convective histories reveals the systematics behind this behavior - at least in the 1D code, if not in nature:

- The little jump at  $M_{\text{He}} = 3.7 M_{\odot}$  ( $M_{\text{ZAMS}} = 13.2 M_{\odot}$ ) from  $M_{\text{Si}} = 1.7 M_{\odot}$  to  $1.6 M_{\odot}$ , reflects the operation of the third convective carbon burning shell. Below this mass, the third shell ignites inside the former full extent of the second shell and outside the effective Chandrasekhar mass. Thus the core oxygen burning start to burn in a smaller extent while this outermost carbon shell operates. For masses above this value, the third shell ignites at the outer boundary of the previous shell and within the Chandrasekhar mass. Core oxygen burning now has to wait until this third shell is complete and therefore the base of this third shell sets (approximately) the extent of the first oxygen convective shell, and thus the base of the second one (Panel 13.45  $M_{\odot}$  of Fig. 14).

- The much larger decrease in  $M_{\text{Si}}$  from  $1.7 M_{\odot}$  to  $1.4 M_{\odot}$  at  $M_{\text{He}} = 4.2 M_{\odot}$  ( $M_{\text{ZAMS}} = 14.6 M_{\odot}$ ) is due to the diminished significance of the second oxygen burning shell. The silicon core shrinks to the extent of the first oxygen burning shell though the second shell continues to be sporadically important for a time (Panel 15.01  $M_{\odot}$  of Fig. 14).
- The jump and wild variations starting at  $M_{\text{He}} = 5.2 M_{\odot}$  and extending up to  $5.7 M_{\odot}$  ( $M_{\text{ZAMS}} = 17.2 M_{\odot}$  to  $19.0 M_{\odot}$ ) mark the transition from convective carbon burning to radiative burning. After the transition near  $\sim 19 M_{\odot}$ , carbon no longer burns exoergically at the center of the star, and there are only two convective shells before oxygen burning rather than three or more. During this transition, carbon core and shell burning vary greatly in location and extent. The large spread in  $M_{\text{Si}}$ , and ultimately in compactness, reflects the irregularity of this transition (Panels 17.90 and 18.81  $M_{\odot}$  of Fig. 14).

Other shell interactions result in the weaker multiple branches seen in higher mass stars in Fig. 8. Despite the specific masses given in the list above, none of these transitions are abrupt and, given slight nudges, the star may oscillate from one to the other solution when it is close to boundaries. This leads to the “multivalued” behavior. Although complicated and probably sensitive to the one-dimensional treatment of the problem, the conclusion is that the presupernova structure in stars from  $13$  to  $19 M_{\odot}$  results from an interplay of convective carbon and oxygen burning shells after carbon ignition.

Putting these various factors together, a deterministic picture emerges. Multiple carbon burning stages - core burning below  $19 M_{\odot}$ , and two or more episodes of shell burning - act to sculpt an entropy distribution in the core so that oxygen shell burning, when it occurs, ignites at and extends to various mass shells. Whether the number of carbon shells is two or three or four and the number of oxygen shells one or two strongly affects the core structure of a presupernova star in the mass range where a significant number of events are observed. These changes in the extent of convective shells, which amplify small differences in the earlier evolution, may end up determining whether the star explodes or makes a black hole.

## 6. COMPACT REMNANTS AND EXPLOSIONS

Since the new models differ from those of Sukhbold & Woosley (2014) and Sukhbold et al. (2016), and to a lesser extent, from Müller et al. (2016), it is worth revisiting some of the conclusions of those papers regarding compact remnants using the new models.

Fig. 15 shows the models now expected to explode based on the criteria of Ertl et al. (2016) and Müller et al. (2016). These figures can be compared with Fig. 4 of Ertl et al. and Fig. 6 of Müller et al., which they very closely resemble. The “N20” engine parameterization was used to make the comparison with Ertl et al. (2016) and the “standard” choices of five parameters were used for Müller et al. (2016) method.

The most significant difference with the Ertl criterion is the shift of the pattern for models above about  $14$

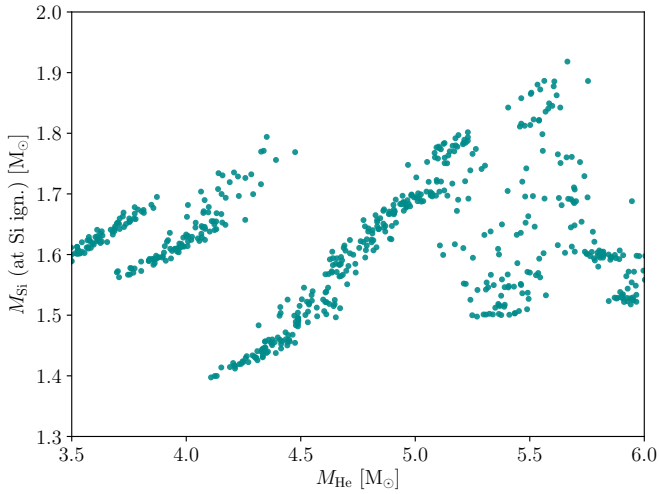


FIG. 13.— The size of the oxygen depleted core (oxygen less than silicon or iron) as a function of helium core mass at silicon ignition (when the central temperature first reaches  $3.0 \times 10^9$  K). This is approximately the maximum extent of the first oxygen convective shell. The function has multiple trajectories that correlate with the major features in the plot of  $M_4$  vs helium core mass in the top panel of Fig. 12.

$M_\odot$  to slightly ( $\sim 10\%$ ) lower masses. Changes in average quantities like the remnant masses are small, however. Fig. 16 shows a comparison of IMF-weighted remnant mass distributions of imploding models assuming a Salpeter (1955) initial mass function with a power of  $-2.35$ . The usual two cases are considered: a) collapse of the helium core, but ejection of the hydrogen envelope; and b) collapse of the entire presupernova star. Case a) is more appropriate for stars where the envelope is lost to a binary companion or, for very massive stars, to winds. The envelope might also be lost to a very weak explosion that did not unbind the helium core (Quataert & Shiode 2012; Fuller 2017; Lovegrove & Woosley 2013). Case b) is for more robust explosions. In each case there is an element of uncertainty because the final mass depends on the mass loss rate, e.g., for red supergiants in Case b) and Wolf-Rayet stars in Case a). In making this Fig. 16, but not in computing the averages, only the mass range covered by our  $\dot{M}_N$  mass loss survey,  $12 - 27 M_\odot$ , was included.

Astronomers, of course, observe black holes coming from all masses of stars, not just  $12 - 27 M_\odot$ . To compute the averages for solar metallicity stars (and the answer will be sensitive to metallicity), the new results were supplemented with the prior models of Sukhbold et al. (2016) for stars more massive than  $27 M_\odot$ . For just the limited mass range  $12 - 27 M_\odot$ , the average black hole masses from Sukhbold et al. (2016) were previously  $6.52$  and  $15.3 M_\odot$  respectively for the helium core and full star assumptions. The corresponding new numbers are  $6.60$  and  $14.2 M_\odot$ . Considering the entire mass range of stars that experience iron core collapse, and using the N20 parameters in Sukhbold et al. (2016), the previous averages were  $9.25 M_\odot$  and  $13.7 M_\odot$ . The equivalent new numbers are  $8.61 M_\odot$  and  $13.5 M_\odot$ . A less than 1% adjustment has been applied to Table 4 of Sukhbold et al. (2016) based upon a slightly different way of interpolating the grid.

Similar corrections can be estimated for the neutron

star gravitational masses. Lacking an explosion model, it is assumed, based on prior experience (i.e., Ertl et al. 2016), that the baryonic mass of the resulting neutron star is usually equal to  $M_4$ . After appropriately correcting for neutrino mass loss (same as in Müller et al. 2016), the new average neutron star gravitational mass in the range  $12 - 27 M_\odot$  is  $1.45 M_\odot$ . Explosions below  $12 M_\odot$  were calculated by Sukhbold et al. (2016) using presupernova models in which the neutrino bug had been fixed. They can thus be combined with the current set. Assuming neutron star production above  $27 M_\odot$  is negligibly small, the new global average neutron star mass is  $1.38 M_\odot$ . In Table 4 of Sukhbold et al. (2016) the corresponding global average was  $1.41 M_\odot$ .

The agreement of Fig. 15 with the earlier work (Fig. 6 of Müller et al. 2016) is excellent, and it is thus expected that the explosion outcomes will also be very similar. Indeed, plots of neutron star mass (Fig. 17), black hole mass, and explosion energy as a function of initial mass (not shown) are virtually indistinguishable from the panels in their Figure 2. This suggests that the difference in envelope structure and zoning between the series of Müller et al. (2016) and the present paper did not have much influence on the core structure and statistical explosion properties.

Fig. 15 shows that a significantly larger fraction of stars in the interesting mass range  $15$  to  $20 M_\odot$  explode using the Müller et al. (2016) formalism, even though "N20" is one of the more energetic formulations of the Ertl et al. (2016) model. Conservatively, this could be regarded as an uncertainty in outcome until more realistic simulations of the actual explosion can be done. The various energies in the Ertl et al. (2016) model came, however, from calibrating a central engine with 1D neutrino transport, a shrinking protoneutron star, and fallback to SN 1987A using various presupernova models and might, for now, be considered the more realistic of the two. This calibration to SN 1987A has its own uncertainties though, especially since the structure of the presupernova star could be different in more realistic binary merger models (e.g., Menon & Heger 2017, and references therein).

Fig. 17 gives the expected neutron star masses that result when our new presupernova models are analyzed using the formalism and standard parameters of Müller et al. (2016). Fallback is neglected in their analysis, so the baryonic mass of the proto-neutron star is equal to the mass coordinate where the neutrino-driven engine shuts off a few hundred ms after shock revival. As mentioned before, this correlates strongly with  $M_4$  (top panel). There are branches of neutron star masses above the  $M_4$  line, which primarily originate from less massive progenitors ( $M_{ZAMS} < 15 M_\odot$ ), reflecting the operation of a prominent second oxygen burning shell and the resulting shallow entropy profile. The most massive neutron stars have a baryonic mass that is bounded by the base of the convective carbon burning shell, which is located much further out than  $M_4$  in the presupernova star. The second panel of Fig. 17 shows the expected neutron star (gravitational) mass as a function of main sequence mass. These results agree quite well with those of Müller et al. (2016, see their Fig. 2c) including the existence of very massive neutron stars produced for main sequence stars  $14 - 15 M_\odot$  and the highly variable nature of the solution between  $14$  and  $19 M_\odot$ . For the majority



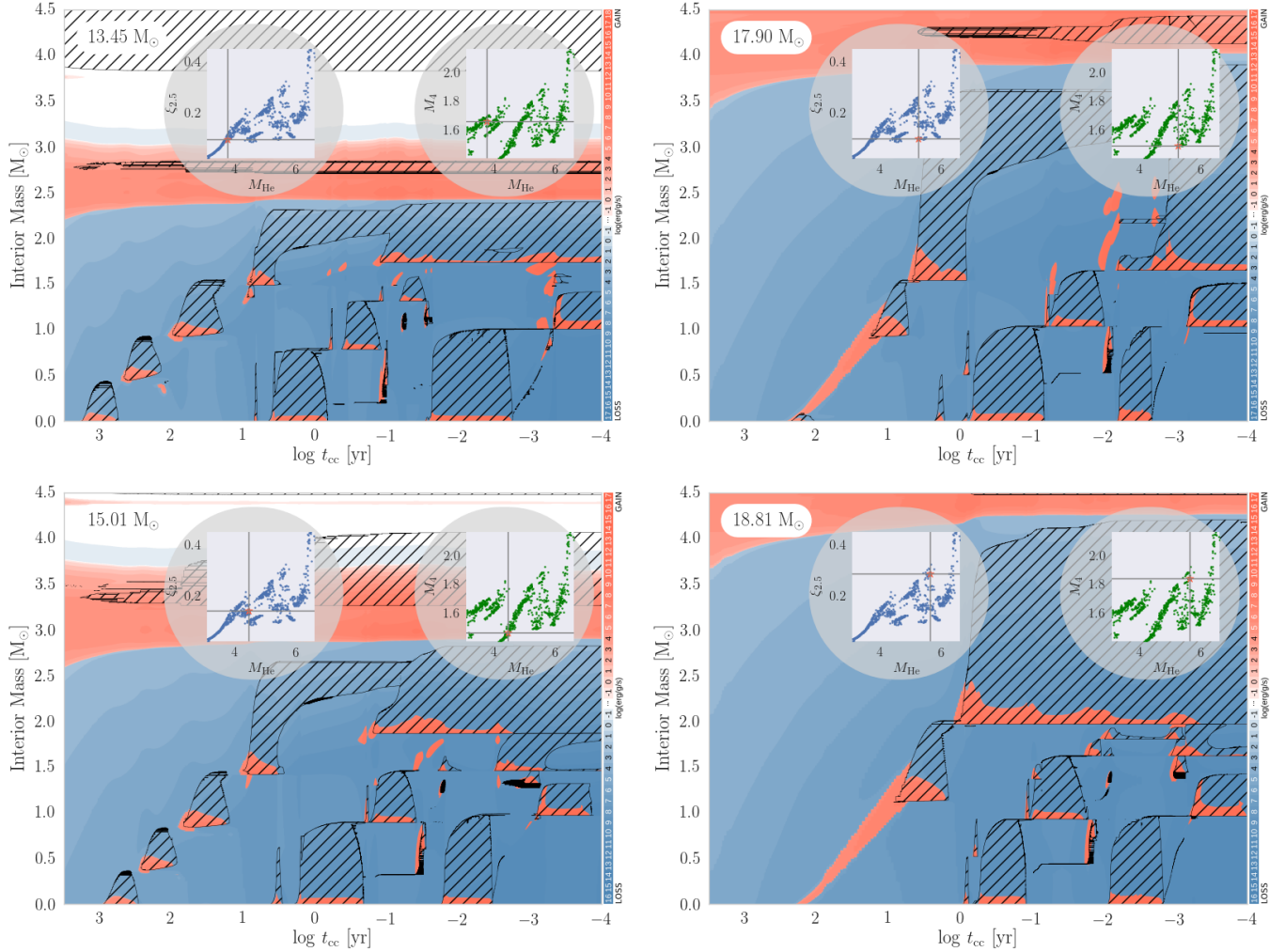


FIG. 14.— Convection histories of four sample models from the range of initial masses from 14 to 19  $M_{\odot}$ , representing key structural changes that are responsible for the significant variations in the final presupernova core properties. Each panel shows the evolution of the innermost 4.5  $M_{\odot}$  material roughly during the last thousand years of its life, i.e., from core carbon burning until presupernova. Colored shades denote energy generation (red) and energy loss (blue) gradients. Hatched black regions are convective episodes. The  $x$ -axis is shown as the log of time until core collapse,  $t_{cc}$ . The initial mass of each model is denoted on the top left of panels. Two inserted mini-plots illustrate the compactness parameter (purple) and the lagrangian location of entropy per baryon equal  $4.0 k_B$  point (green) respectively, both as a function of helium core mass corresponding to the above mentioned initial mass range. The crosses inside each mini-plots denote the values corresponding to the model. (13.45  $M_{\odot}$ ;) The lowest mass stars have 4 or more convective carbon burning episodes followed by 3 oxygen burning episodes (including central core burning episode). The shell helium burning lies within the 2.5  $M_{\odot}$  location, the point on which the compactness parameter,  $\xi_{2.5}$ , is measured, and thus these models have small compactness and small  $M_4$ . (15.01  $M_{\odot}$ ;) Central carbon burning weakens with increasing mass, and as a result the shell carbon burning episodes gradually “migrate” inwards (with increasing initial mass). Once the third shell carbon burning ignites within the effective Chandrasekhar mass, the core oxygen burning has to wait until the overlying carbon burning episode is finished, which leads to significantly weakened or, in some cases absent, immediate second oxygen shell burning. In these models oxygen eventually burns later when silicon is already ignited in the core. This marks the transition of  $M_4$  to the “second” branch. Due to its sensitivity to the last major shell burning episode, the compactness parameter has multiple solutions depending on the final configuration of oxygen, neon and carbon burning (i.e. together burn vigorously in one shell, or separately). (17.90  $M_{\odot}$ ;) Around  $\sim 18 M_{\odot}$  it becomes increasingly harder for carbon to burn convectively near the center. The tiny convective central burning episode is followed by a long lasting radiative flame, and as a result, with increasing initial mass, the base of the convective carbon burning shells start to migrate outwards. (18.81  $M_{\odot}$ ;) Eventually at high enough initial mass all central carbon burning is radiative. Models between 17 and 19  $M_{\odot}$  have rapidly changing core structures, and thus rapidly varying  $\xi_{2.5}$  and  $M_4$ . Same format plots for all 800 models between 12.00 and 19.99  $M_{\odot}$  are available online (see Footnote 9).

of models, the resulting neutron star mass is tightly correlated with  $M_4$  (Fig. 12) and oxygen depleted core at the time of silicon ignition (Fig. 13), and in certain initial mass ranges the explosion of models with nearly identical mass (or slightly different input physics) can result in very different neutron stars.

It is not expected that the nucleosynthesis and light curves calculated by Sukhbold et al. (2016) will be significantly altered by using the new models, though further

exploration is certainly encouraged. In particular, the deficiency of light  $s$ -process elements seen in Sukhbold et al. (2016) will persist in the new model set, since most of the production of these elements is due to the most massive stars (Brown & Woosley 2013) which still fail to explode. The fraction of solar metallicity stars above 9  $M_{\odot}$  exploding as supernovae was 74% based on the N20 parameterization (Table 4 of Sukhbold et al. 2016) and is now 65%. Above 18  $M_{\odot}$ , the fraction of SN reduces

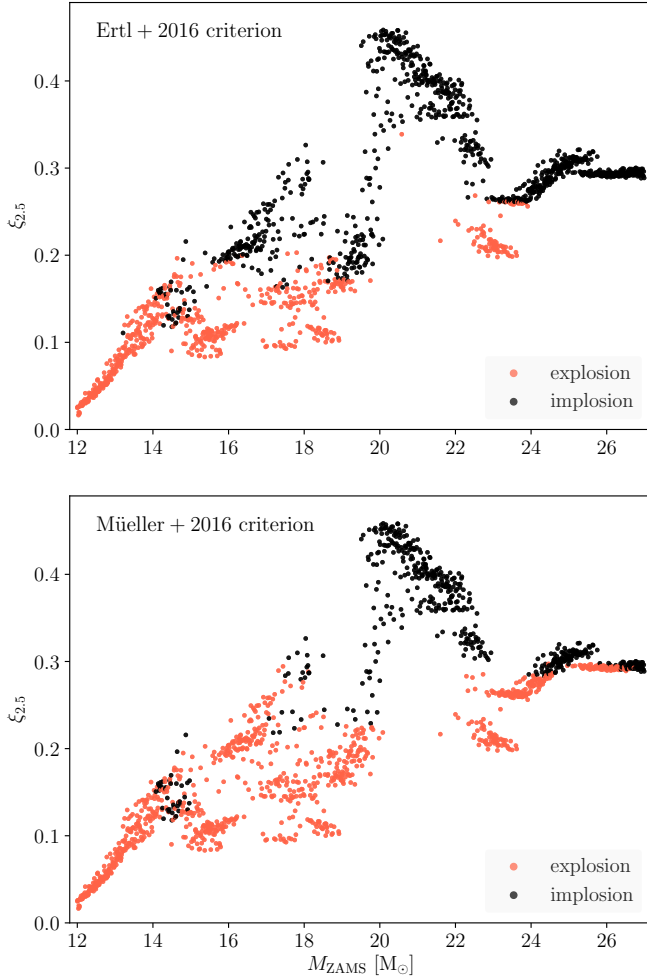


FIG. 15.— The compactness parameter shown in Fig. 8 is plotted again twice, color coded as to the success or failure of the explosion based upon the parameterization of Ertl et al. (2016) (top) and the semi-analytical method of Müller et al. (2016) (bottom). Red symbols denote successful explosions by these criteria, and black symbols, failures. The very good agreement between these two different approaches suggests that both are good representations of core structure, though the criterion of Müller et al. (2016) favors slightly more explosions for the parameters chosen.

to only 8%, which actually is in a slightly better accord with the results from Smartt (2009, 2015), as compared to the previous study. Since the envelope masses have not changed appreciably and the explosion energies are also expected to be unchanged, the light curves will be unaltered. The fractions given in their Table 4 for supernovae above 12, 20, and 30  $M_{\odot}$  will also probably not change within the variations already seen for the different central engine characteristics.

## 7. CONCLUSIONS

The full evolution of over 4,000 massive stars of solar metallicity in the mass range 12 to 60  $M_{\odot}$  has been studied using unprecedented resolution, both in zones per star and number of stars within a given mass range. The mass loss rate was varied, and an important bug in the neutrino loss routine was repaired that caused a significant variation in the presupernova properties from those calculated by Sukhbold & Woosley (2014) and prior works. Our chief conclusions are:

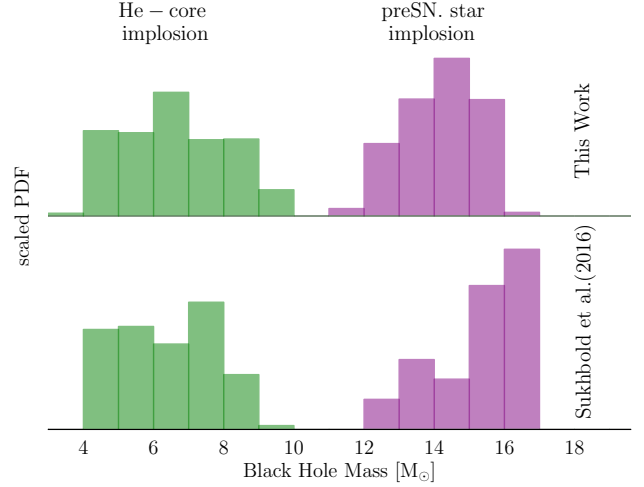


FIG. 16.— The IMF-weighted black hole mass distributions for the new  $\dot{M}_N$  set is shown in comparison with the results from Sukhbold et al. (2016) over the same initial mass range between 12 and 27  $M_{\odot}$ . The differences are small and well within the range of variation seen for different explosion models. The average black hole masses for the older study is 15.3 and 6.52  $M_{\odot}$  for two scenarios respectively, while the new models yield 14.2 and 6.60  $M_{\odot}$ .

- The pattern of core compactness seen in previous studies (e.g., Sukhbold & Woosley 2014; Müller et al. 2016) is robust. The “noise” in these studies was not a consequence of inadequate zoning, but reflects real variability. The range of variation and the location of peaks (Fig. 8) in the new study are virtually identical to that seen by Müller et al. (2016), even though the new models use 4 to 10 times the zoning and a much smaller surface boundary pressure. The results are also qualitatively similar to Sukhbold & Woosley (2014), but important peaks in the compactness plot are shifted downwards by about 10 % in initial mass (Fig. 9) due to the corrected neutrino loss rate. For the stellar physics used and spherically symmetric nature of the calculation, the variations and peaks seen in Fig. 8 are now well determined.
- The large variation in core structure seen for stars between 14 and 19  $M_{\odot}$  by Sukhbold & Woosley (2014) is not completely random. For a larger set of models with finer spacing in initial mass, several branches of solutions emerge. This behavior was also seen by Müller et al. (2016). The branches apparently result from variations in the location of the oxygen burning shells in the presupernova star, which in turn “remember” the location of several carbon burning shells of variable extent. Some noise is introduced by the fact that the carbon abundance and size of the carbon-oxygen core are not precisely monotonic with mass (Fig. 7). This, in turn, reflects the operation of semiconvection at the boundary of the hydrogen and helium convective core. In the mass ranges 14 to 19  $M_{\odot}$  and 22 to 24  $M_{\odot}$ , the presupernova core structure is more sensitive to events in the last year of a star’s life (and sometimes the last hours) than to the star’s initial mass. Presupernova structure in these mass ranges does not necessarily follow the Vogt-Russell

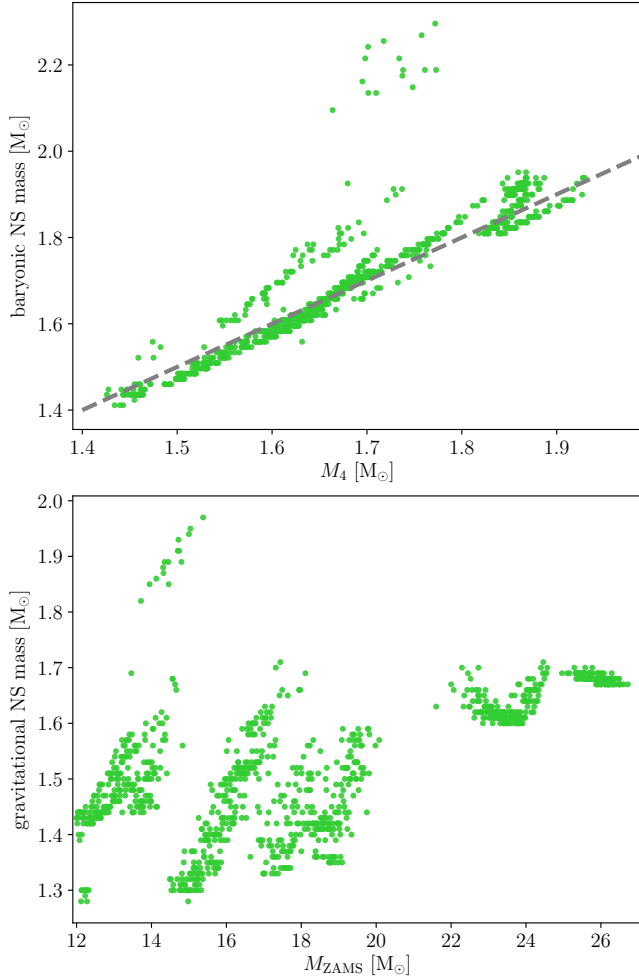


FIG. 17.— Neutron star mass distribution resulting from analyzing the new model set with normal mass loss ( $\dot{M}_N$ ) for stars in the mass range 12 to 27  $M_\odot$  using the approach of Müller et al. (2016). (Top:) The baryonic mass of the expected neutron star is plotted as a function of  $M_4$ , the mass where the entropy per baryon reaches  $4.0k_B$  in the presupernova star (§5). Neutron stars on the grey dashed line have a mass, before neutrino losses, equal to  $M_4$ . Many points are found here because  $M_4$  is usually the “mass cut” in a successful explosion, unless the final entropy profile is significantly more shallow. (Bottom:) The gravitational mass (adjusted from the baryonic mass in the same way as in Müller et al. 2016) of the expected neutron star as a function of main sequence mass. More massive neutron stars are typically made by more massive main sequence stars with a greater  $\xi_{2.5}$  and  $\mu_4$ , but the most massive points on this plot come from models with  $M_{ZAMS} \sim 14 - 15 M_\odot$ , the most massive models with a significant second oxygen shell burning. The existence of multiple branches for these quantities (Fig. 12 and Fig. 13) results in a large range of neutron star masses being accessible by stars of nearly the same main sequence mass for some initial masses. Note also the cluster of neutron stars with mass near 1.65  $M_\odot$  coming from the most massive supernova progenitors.

theorem (Vogt 1926; Russell 1927). It may be more comparable to weather on earth.

- Even accounting for these systematics, the branches of solutions are still noisy. The level of noise is reduced if one characterizes the presupernova star by its helium core mass, not its starting mass or final total mass. The scatter is also reduced in the Ertl two-parameter characterization of core-structure rather than the O’Connor-Ott compact-

ness parameter.

- Given the large number of models, it is possible to give statistically meaningful results for the radius, luminosity and effective temperature of supernova progenitors (§4.1).
- The mass distributions of neutron stars and black holes resulting from supernovae in the mass range studied are not greatly altered from our earlier surveys (§6). The average gravitational mass of neutron stars, including all masses of supernovae, is now 1.38  $M_\odot$ . The average black hole mass, if only the helium core implodes, is 8.61  $M_\odot$ . If the entire presupernova star collapses, the average black hole mass is 13.5  $M_\odot$ . The fraction of stars above 9  $M_\odot$  that explode rather than collapsing is estimated to be 65%. The fraction above 18  $M_\odot$  is 8%. Nucleosynthesis and light curves are basically unchanged.

Binary mass exchange and rotation undoubtedly play key roles, but have been neglected in this study. To first order, stars that end up with the same final helium core mass will have similar presupernova compactness and fates. Similar systematic variations and multi-valued solutions are expected to persist. The statistical averages of compact remnant masses may vary, however, and certainly the light curves will be different. Our models are publically available to those wanting to estimate outcomes based upon their own distribution of helium core masses, carbon-oxygen core masses, etc. In the future, we will consider rotating models, but this was principally a study of how resolution affects the solution to a well-defined, frequently studied problem.

Our results suggest a slightly different strategy to the study of presupernova evolution and supernova modeling than sometimes used in the past. Given the variation in outcome for stars of nearly the same mass, or the same mass with different codes, a statistically meaningful sample of models must be calculated before drawing strong conclusions about supernova mass ranges, remnant mass distributions, nucleosynthesis, etc. Historically, researchers have sometimes focused on the calculation of just a few masses, e.g., 15, 20, 25  $M_\odot$ , and sought to test the sensitivity to changes in physics in just those cases. Here we see that calculating a statistically meaningful sample may be just as important as getting the physics precisely right. The size of such a sample depends upon the need to resolve regions of rapid variability found with a given code and physics, but a minimum initial mass grid of 0.1  $M_\odot$  is reasonable within such regions.

Some of the models calculated here had merged carbon and oxygen convective shells at the end. Many did not. Others were only separated by a single thin zone from being coupled. Similar to the numerical artifact seen when helium burning is calculated with too little semiconvection, these mathematical bifurcations may not be real and might be overcome, or at least smoothed out (Alexakis et al. 2004), by increasing the convective overshoot or doing a multi-dimensional calculation (e.g., Meakin & Arnett 2007; Viallet et al. 2013; Arnett & Meakin 2016; Jones et al. 2017; Cristini et al. 2017).



In general, linked convective shells give a more compact core structure and favor explosions (see, e.g., Collins et al. 2017). Further study with other representations of convective overshoot mixing and multi-dimensional codes are thus encouraged.

Semiconvection and overshoot mixing remain major uncertainties in studies of this sort and also play important roles in determining the helium and carbon-oxygen core masses. How KEPLER treats semiconvection is described in Weaver & Woosley (1993). It is expected that other studies using different treatments will find results that differ in important detail from those presented here. The overall pattern, multi-peaked structure and range of variability of the compactness parameter and other measures of core structure should persist, however. Clusters of solutions due to variable numbers and extents of the carbon and oxygen shells should also be a common feature. Further exploration is again encouraged.

All of the new presupernova models presented here are available online. Also online are plots of the convective histories of 800 models between 12 and 20  $M_{\odot}$  of the  $\bar{M}$  set (see Footnote 9). Other auxiliary presupernova models (e.g., those presented in §2.1 and §2.2) are available upon request to the authors.

#### ACKNOWLEDGMENTS

We thank Raphael Hirschi for a careful review of this work and for providing many useful suggestions. We also thank Bernhard Müller for helping us to process our new progenitor results through his semi-analytical explosion modelling and feedback on this manuscript. Thomas Janka and Thomas Ertl provided valuable insight into the supernova explosion models and their dependence on progenitor properties. We thank Todd Thompson and John Beacom for useful comments on the manuscript. We also appreciate the efforts of Gang Gao in discovering the neutrino bug in the KEPLER code. All numerical KEPLER calculations presented in this work were performed on the RUBY cluster at the Ohio Supercomputer Center (Ohio Supercomputer Center 1987). TS is partly supported by NSF PHY-1404311 to John Beacom. SW is supported by NASA NNX14AH34G. AH is supported by an ARC Future Fellowship, FT120100363, and, in part, by the National Science Foundation under Grant No. PHY-1430152 (JINA Center for the Evolution of the Elements).

## REFERENCES

- Alexakis, A., Calder, A. C., Heger, A., Brown, et al. 2004, *ApJ*, 602, 931
- Appenzeller, I. 1970, *A&A*, 5, 355
- Arnett, W. D., & Meakin, C. 2016, *Reports on Progress in Physics*, 79, 102901
- Asplund, M., Grevesse, N., Sauval, A. J., & Scott, P. 2009, *ARA&A*, 47, 481
- Barkat, Z. 1994, *Supernovae*, 31
- Beasor, E. R., & Davies, B. 2018, *MNRAS*, 475, 55
- Brown, J. M., & Woosley, S. E. 2013, *ApJ*, 769, 99
- Buchmann, L. 1996, *ApJ*, 468, L127
- Burrows, A., & Lattimer, J. M. 1987, *ApJ*, 318, L63
- Chieffi, A., & Straniero, O. 1989, *ApJS*, 71, 47
- Collins, C., Müller, B., Heger, A. 2017, *MNRAS*, submitted; arXiv/170900236
- Cristini, A., Meakin, C., Hirschi, R., et al. 2017, *MNRAS*, 471, 279
- Davies, B., Kudritzki, R.-P., Plez, B., et al. 2013, *ApJ*, 767, 3
- Ertl, T., Janka, H.-T., Woosley, S. E., Sukhbold, T., & Ugliano, M. 2016, *ApJ*, 818, 124
- Farmer, R., Fields, C. E., Petermann, I., et al. 2016, *ApJS*, 227, 22
- Fryer, C. L. 1999, *ApJ*, 522, 413
- Fuller, J. 2017, *MNRAS*, 470, 1642
- Heger, A. 1998, Ph.D. Thesis,
- Heger, A., Langer, N., Woosley, S.E. 2000, *ApJ*, 52, 368
- Itoh, N., Hayashi, H., Nishikawa, A., & Kohyama, Y. 1996, *ApJS*, 102, 411
- Jones, S., Androssy, R., Sandalski, S., et al. 2017, *MNRAS*, 465, 2991
- Lauterborn, D., Refsdal, S., & Weigert, A. 1971, *A&A*, 10, 97
- Levesque, E. M., Massey, P., Olsen, K. A. G., et al. 2005, *ApJ*, 628, 973
- Lovegrove, E., & Woosley, S. E. 2013, *ApJ*, 769, 109
- Meakin, C. A., & Arnett, D. 2007, *ApJ*, 667, 448
- Meibom, A., Krot, A. N., Robert, F., et al. 2007, *ApJ*, 656, L33
- Menon, A., & Heger, A. 2017, *MNRAS*, 4649-4664, 469
- Müller, B., Heger, A., Liptai, D., & Cameron, J. B. 2016, *MNRAS*, 460, 742
- Nieuwenhuijzen, H., & de Jager, C. 1990, *A&A*, 231, 134
- Ohio Supercomputer Center 1987, Ohio Supercomputer Center, <http://osc.edu/ark:/19495/f5s1ph73>
- O'Connor, E., & Ott, C. D. 2011, *ApJ*, 730, 70
- O'Connor, E., & Ott, C. D. 2013, *ApJ*, 762, 126
- Paxton, B., Bildsten, L., Dotter, A., et al. 2011, *ApJS*, 192, 3
- Paxton, B., Marchant, P., Schwab, J., et al. 2015, *ApJS*, 220, 15
- Pejcha, O., & Thompson, T. A. 2015, *ApJ*, 801, 90
- Quataert, E., & Shiode, J. 2012, *MNRAS*, 423, L92
- Rauscher, T., Heger, A., Hoffman, R. D., & Woosley, S. E. 2002, *ApJ*, 576, 323
- Renzo, M., Ott, C. D., Shore, S. N., & de Mink, S. E. 2017, *A&A*, 603, A118
- Russell, H. N. 1917, in *Astronomy*, Vol 2, by H. N. Norris, R. S. Dugan, and J. Q. Stewart, Ginn and Co., Boston, p 910
- Salpeter, E. E. 1955, *ApJ*, 121, 161
- Sanyal, D., Langer, N., Szécsi, D., -C Yoon, S., & Grassitelli, L. 2017, *A&A*, 597, A71
- Sanyal, D., Grassitelli, L., Langer, N., & Bestenlehner, J. M. 2015, *A&A*, 580, A20
- Smartt, S. J. 2009, *ARA&A*, 47, 63
- Smartt, S. J. 2015, *Pub. Astron. Soc. Australia*, 32, e016
- Sukhbold, T., & Woosley, S. E. 2014, *ApJ*, 783, 10
- Sukhbold, T., Ertl, T., Woosley, S. E., Brown, J. M., & Janka, H.-T. 2016, *ApJ*, 821, 38
- Sukhbold, T. 2016, Ph.D. Thesis,
- Timmes, F. X., Woosley, S. E., & Weaver, T. A. 1996, *ApJ*, 457, 834
- Tur, C., Heger, A., & Austin, S. M. 2007, *ApJ*, 671, 821
- Ugliano, M., Janka, H.-T., Marek, A., & Arcones, A. 2012, *ApJ*, 757, 69
- Viallet, M., Meakin, C., Arnett, D., & Mocák, M. 2013, *ApJ*, 769, 1
- Vogt, H. 1926, *Astronomische Nachrichten*, 226, 301
- Weaver, T. A., Zimmerman, G. B., & Woosley 1978, *ApJ*, 225, 1021
- Weaver, T. A., & Woosley, S. E. 1993, *Phys. Rep.*, 227, 65
- Woosley, S. E., Heger, A., & Weaver, T. A. 2002, *Reviews of Modern Physics*, 74, 1015
- Woosley, S. E., Heger, A., Cumming, A., et al. 2004, *ApJS*, 151, 75
- Woosley, S. E., & Heger, A. 2007, *Phys. Rep.*, 442, 269
- Woosley, S. E., & Heger, A. 2015, *ApJ*, 810, 34
- Woosley, S. E. 2017, *ApJ*, 836, 244